

Introducing the TNG-Cluster Simulation: overview and physical properties of the gaseous intracluster medium

Dylan Nelson¹*, Annalisa Pillepich², Mohammadreza Ayromlou¹, Wonki Lee^{4,5}, Katrin Lehle¹, Eric Rohr², and Nhut Truong^{3,2}

¹ Universität Heidelberg, Zentrum für Astronomie, ITA, Albert-Ueberle-Str. 2, 69120 Heidelberg, Germany

² Max-Planck-Institut für Astronomie, Königstuhl 17, 69117 Heidelberg, Germany

³ NASA/Goddard Space Flight Center, Greenbelt, MD 20771, USA

⁴ Yonsei University, Department of Astronomy, Seoul, Republic of Korea

⁵ Harvard-Smithsonian Center for Astrophysics, 60 Garden Street, Cambridge, MA, 02138, USA

ABSTRACT

We introduce the new TNG-Cluster project, an addition to the IllustrisTNG suite of cosmological magnetohydrodynamical simulations of galaxy formation. Our objective is to significantly increase the statistical sampling of the most massive and rare objects in the Universe: galaxy clusters with $\log(M_{200c}/M_\odot) \gtrsim 14.3 - 15.4$ at $z = 0$. To do so, we re-simulate 352 cluster regions drawn from a 1 Gpc volume, thirty-six times larger than TNG300, keeping entirely fixed the IllustrisTNG physical model as well as the numerical resolution. This new sample of hundreds of massive galaxy clusters enables studies of the assembly of high-mass ellipticals and their supermassive black holes (SMBHs), brightest cluster galaxies (BCGs), satellite galaxy evolution and environmental processes, jellyfish galaxies, intracluster medium (ICM) properties, cooling and active galactic nuclei (AGN) feedback, mergers and relaxedness, magnetic field amplification, chemical enrichment, and the galaxy-halo connection at the high-mass end, with observables from the optical to radio synchrotron and the Sunyaev-Zeldovich (SZ) effect, to X-ray emission, as well as their cosmological applications. We present an overview of the simulation, the cluster sample, selected comparisons to data, and a first look at the diversity and physical properties of our simulated clusters and their hot ICM.

Key words. galaxies: clusters – galaxies: clusters: intracluster medium – galaxies: evolution – galaxies: formation – galaxies: halos

1. Introduction

Galaxy clusters are the ultimate outcome of the hierarchical assembly of structure in the standard cosmological framework, Λ CDM. Their stellar bodies, supermassive black holes (SMBHs), dark matter halos, and gaseous atmospheres are all constructed from the collective merging of thousands, if not tens of thousands, of smaller constituents. Clusters are the most massive virialized structures in the Universe. They host the most massive galaxies, the most massive SMBHs, and the largest populations of satellite galaxies. The dynamics and physical processes at play in the hot plasma of the intracluster medium (ICM) are complex, diverse, and observable. Clusters are cosmologically rare, yet provide a key observational probe of our cosmological model.

The hot, ionized gas of the ICM can be studied across a number of multi-wavelength tracers, from cluster cores to their outskirts (Reiprich et al. 2013). These include X-ray emission (Pratt et al. 2009; Vikhlinin et al. 2009) with instruments such as Chandra, XMM-Newton, and Suzaku (Bautz et al. 2009; Sato et al. 2012), plus all-sky surveys from ROSAT and now eROSITA (Merloni et al. 2012). Future X-ray imaging spectrometers including the recently launched XRISM (XRISM Science Team 2020), the Line Emission Mapper (LEM; Kraft et al. 2022), and ATHENA X-IFU (Nandra et al. 2013) will reveal the kinematics and physical properties of this hot gas (Simionescu et al. 2019).

The ionized ICM also imprints the SZ effect (Sunyaev & Zeldovich 1970), quantified to great success over the past decade with survey machines including Planck, ACT, and SPT (Planck Collaboration et al. 2014). Future high spatial resolution obser-

vations of the SZ effect in the ICM will reveal new intracluster physics (Romero et al. 2017; Mroczkowski et al. 2019), e.g. with ALMA (Kitayama et al. 2023), NIKA2 (Perotto et al. 2022), and TolTEC (Montaño et al. 2019), plus survey-scale programs including CMB-S4 (Raghunathan et al. 2022) and Simons Observatory (SO; Ade et al. 2019a). The ICM is also visible at radio wavelengths due to synchrotron emission from relativistic particle populations. This tracer has led to recent discoveries with LOFAR (radio megahalos; Cuciti et al. 2022) and MeerKAT (Knowles et al. 2022).

The ICM is not exclusively hot: it is a multi-phase gaseous halo also observed to contain cooler phases such as H α (Fabian et al. 2003; Crawford et al. 2005), MgII (Anand et al. 2022), and even molecular CO (Salomé et al. 2006). Cool gas in cluster cores is, perhaps surprisingly, common, at least in some systems (Olivares et al. 2019). Indeed, the central thermodynamical properties of clusters suggest a possible dichotomy, and/or diversity, between ‘cool-core’ and ‘non-cool-core’ clusters (McCarthy et al. 2004; Cavagnolo et al. 2008; Rafferty et al. 2008).

At all halo mass scales, astrophysical feedback processes within galaxies imprint signatures in the physical properties, and observables, of hot halos (Nelson et al. 2018a; Truong et al. 2020, 2021; Oppenheimer et al. 2020; Ayromlou et al. 2023a). In clusters, accreting SMBHs i.e. active galactic nuclei (AGN) inject large amounts of feedback energy into the inner ICM (Hlavacek-Larrondo et al. 2022). As a result, cluster thermodynamics are set by physics beyond gravitational dynamics alone (Valageas & Silk 1999; Wu et al. 2000; Lewis et al. 2000; Babul et al. 2002). The observational manifestations of AGN feedback in clusters include relativistic and radio-emitting jets, together with asso-

* E-mail: dnelson@uni-heidelberg.de

ciated cavities/bubbles visible in X-ray emission (Fabian 2012). These heating sources offset radiative cooling in the ICM (Voit et al. 2005) and lead to an approximate global thermal balance, preventing runaway cooling flows (McNamara & Nulsen 2012).

As a result, the brightest central/cluster galaxies (BCGs) that form at the centers of clusters are predominantly massive, quenched, ellipticals (De Lucia & Blaizot 2007). These galaxies have recent formation (i.e. assembly) redshifts, yet are primarily built via accreted, ex-situ stars which have formed already at $z \gtrsim 2$ (Rodriguez-Gomez et al. 2015; Thomas et al. 2010). Their stellar light extends for hundreds of kilo parsecs, producing the intra-cluster light (ICL; Lin & Mohr 2004). Clusters host the heaviest SMBHs in the Universe, with $M \gtrsim 10^{10} M_\odot$ (van den Bosch et al. 2012). These are radiatively inefficient, low accretion rate SMBHs preferentially in the centers of cool-core clusters (Hlavacek-Larrondo & Fabian 2011).

Clusters are also observed to contain hundreds or even thousands of luminous satellite galaxies (Hansen et al. 2009). Galaxy evolution within clusters produces strong environmental effects including ram-pressure and tidal stripping (Moore et al. 1996; Yun et al. 2019; Rohr et al. 2023b), quenching (Wetzel et al. 2013), and morphological transformation (Dressler 1980). Satellite properties are biased with respect to their field counterparts, in star formation activity and colors (Kauffmann et al. 2004), metallicity (Pasquali et al. 2010), and stellar to (sub)halo mass ratio (Niemicc et al. 2017), indicative of environmental effects. Satellite galaxy populations in high-mass host halos therefore probe a broad range of physical processes (Bahé & McCarthy 2015; Ayromlou et al. 2019; Martín-Navarro et al. 2021).

Clusters have typically been observed at low redshift, where they can be detected in abundance and characterized in detail. However, their progenitors at $z \gtrsim 1 - 2$ reveal the assembly of these rare overdensities (Overzier 2016). Massive protoclusters have already formed their hot ICM by $z \sim 2$ (Di Mascolo et al. 2023), and the cooler gas phases in and around protoclusters may produce observed large-scale Lyman alpha emission (Steidel et al. 2000; Byrohl & Nelson 2023). At earlier evolutionary stages, prior to virialization, protoclusters are characterized by numerous individual galaxies evolving within a large-scale overdensity of the cosmic web. Galaxies in such dense regions have preferentially early formation redshifts and experience strong environmental effects (Thomas et al. 2005; Postman et al. 2005). At even earlier times, during the epoch of the first galaxies, protoclusters likely host the most massive galaxies that exist, as now being detected at $z \gtrsim 6$ in the JWST era (Labbé et al. 2023; Looser et al. 2023; Lovell et al. 2023).

The multi-wavelength characterization and modeling of galaxy clusters have become a central theme of recent large survey programs (CHEX-MATE Collaboration et al. 2021). Cluster samples have been assembled using a variety of observational tracers, based on their constituent gas (mainly X-ray and SZ), stars (optical), and dark matter (weak lensing). It is now appreciated that strong selection functions, particularly with X-ray selected samples, may have biased our view of galaxy cluster physics (Donahue et al. 2001; Rossetti et al. 2016, 2017; Lovisari et al. 2017; Popesso et al. 2023). Potential biases are also critical if clusters are to be used as cosmological probes.

A cornerstone of precision cosmology is the detection and characterization of galaxy clusters, across the electromagnetic spectrum (Allen et al. 2011). In the microwave, for example, Simons Observatory (SO) will detect tens of thousands of clusters via the thermal and kinetic SZ effects, enabling cosmological parameter constraints from tSZ cluster counts (Ade et al. 2019b). All uses of galaxy clusters for cosmology are limited by theoretical

uncertainties in mapping from observable properties of clusters to total halo mass (mass-observable relations; e.g. Zhang et al. 2008, 2010; Vikhlinin et al. 2009; Hoekstra et al. 2015; Mantz et al. 2016). In the optical, the recently launched Euclid mission will measure the abundance and properties of clusters as cosmological probes (Amendola et al. 2018). In the X-ray, the eROSITA all-sky survey telescope will use cluster number counts for Stage IV cosmological parameter constraints (Pillepich et al. 2012). Achieving these goals requires cosmological hydrodynamical simulations, which can produce high realism synthetic observations through forward modeling, while self-consistently accounting for the complexities of cluster baryonic physics such as feedback.

This is a challenging task. Despite their broad observational importance and extensive characterization, our theoretical understanding of clusters is far from complete (Kravtsov & Borgani 2012). In part, this is because the evolution of the baryonic content of these halos is subject to a complex interplay of gravitational, (magneto)hydrodynamical, radiative, and chemical processes (Donahue & Voit 2022). Clusters are baryonically closed systems (Ayromlou et al. 2023a), but this does not imply they are static. Their virial shocks are located at $\sim 2 - 3 \times r_{\text{vir}}$ (Voit et al. 2003), the extent of the hot ICM (Molnar et al. 2009; Vazza et al. 2010; Zinger et al. 2018). Gas inflows from the intergalactic medium into clusters – cosmic accretion – often in the form of large-scale filaments (Malavasi et al. 2023).

In the opposite direction, and fighting against the gravitational potential well, feedback-driven outflows can reshape gaseous halos. In clusters, AGN can launch powerful outflows, in the form of relativistic jets (Blandford et al. 2019) and high-velocity winds (Yuan & Narayan 2014). The physical drivers behind AGN feedback remain an ongoing topic of study (Liska et al. 2022). The relationship of AGN feedback to the structure, morphology, and evolution of the gaseous ICM is likewise an active area of research (Werner et al. 2019; Altamura et al. 2023).

In addition to feedback, cosmic structure formation also produces complex gas kinematics in the ICM. Mergers of substructure (i.e. other halos) drive halo-scale motions and turbulence (Iapichino & Brüggen 2012). The resulting cascade of energy to small scales produces observable velocity structure (Hitomi Collaboration et al. 2018) and amplifies magnetic fields via the turbulent dynamo (Kazantsev 1968). All contribute non-thermal support to cluster atmospheres, producing a so-called hydrostatic bias (Miralda-Escude & Babul 1995). Capturing the interplay of such a broad range of physical ingredients is non-trivial.

To model the complex and non-linear interactions between the relevant physical processes in clusters requires numerical calculations (Katz & White 1993; Evrard et al. 1994; Eke et al. 1998). Simulations of galaxy clusters are, however, challenging. Their large masses and volumes make high mass or spatial resolution computationally expensive, but as end-products of hierarchical assembly, they are built up from smaller galaxies and halos, making high resolution mandatory. Beyond resolution, accurate solvers and numerical methods for galaxy cluster physics also remain a computational challenge (ZuHone et al. 2015; Kannan et al. 2017; Ehlert et al. 2018; Steinwandel et al. 2023).

There are many cosmological hydrodynamical simulation projects focused on galaxy clusters with $M_{200c} > 10^{14} M_\odot$. Simulations with high $\sim 10^6 M_\odot$ baryon resolution, similar to typical large-volume cosmological boxes, include Hydrangea (Bahé et al. 2017) and C-EAGLE (Barnes et al. 2017a). Current $\sim (100 \text{ Mpc})^3$ large-volume simulations at this resolution such as Illustris, EAGLE, TNG100, and SIMBA all contain a handful of such high-mass halos. Simulations of clusters with even better

$\lesssim 10^5 M_\odot$ baryon resolution, required to model smaller satellite systems, are prohibitively expensive, and only the $\sim 10^{14} M_\odot$ clusters from TNG50 (Pillepich et al. 2019; Nelson et al. 2019a) and Romulus-C (Tremmel et al. 2018) exist.

At the $\sim 10^7 - 10^8 M_\odot$ baryon resolution level there are large-volume simulations such as TNG300, Magneticum 2hr (Dolag et al. 2016), and the recent MillenniumTNG (Pakmor et al. 2023b) and FLAMINGO (Schaye et al. 2023) simulations, and numerous zoom suites including Rhapsody-G (Hahn et al. 2017), DI-ANOVA (Rasia et al. 2015; Bassini et al. 2020), YZiCS (Choi & Yi 2017), and The Three Hundred (Cui et al. 2018, 2022, including realizations with multiple galaxy formation models). At lower $\gtrsim 10^9 M_\odot$ baryon resolution, simulations no longer capture galaxy formation physics, and are often aimed at large-scale and cosmological applications, e.g. MACSIS (Barnes et al. 2017b), cosmo-OWLS (Le Brun et al. 2014), and BAHAMAS (McCarthy et al. 2017). Of all these projects, we note that The Three Hundred is most similar to TNG-Cluster in its approach and objectives.

However, there are significant differences in the cluster simulation projects above, beyond numerical resolution alone. In particular, the statistics i.e. sample sizes, numerical methodologies, and range of included physics all vary considerably. In order to simulate galaxies, and galaxy clusters, the adopted physical model is crucial. For example, some previous cosmological cluster simulations, including ‘non-radiative’ models, neglect black hole feedback from a central engine. Without SMBH feedback galaxy formation at the high-mass end is widely unrealistic, and the properties of the ICM may become unreliable. Overall, the range of scientific applications and science questions that can be addressed with a given galaxy cluster simulation depends on its scope, realism, and physical richness.

Here we introduce a new large simulation project, TNG-Cluster.¹ This is a suite of fully cosmological galaxy cluster simulations, including magnetohydrodynamics and the complete baryonic physics model of the IllustrisTNG simulation project. We simulate 352 high-mass halos with $M_{200c} \sim 10^{14.5-15.4} M_\odot$ down to $z = 0$, with three principal scientific goals: (i) to understand the gas physics of the ICM, (ii) to provide the necessary observables for precision cosmology in the next decade, and (iii) to explore the assembly of the most massive galaxies, their SMBHs, and their surrounding satellite galaxy populations.

In this introductory paper we give an overview of TNG-Cluster and its outcomes. In a series of companion papers we further showcase first science results from TNG-Cluster: a census of ICM kinematics (Ayromlou et al. 2023b), their inference mock X-ray spectroscopic observations (e.g. XRISM/LEM; Truong et al. 2023), the realization of cool-core and non cool-core systems (Lehle et al. 2023), the circumgalactic medium by cluster massive satellites (Rohr et al. 2023a) and the formation of radio relics in massive mergers (Lee et al. 2023). The TNG-Cluster simulation will be made publicly available in the future (Pillepich et al. in preparation).

This paper is structured as follows. Section 2 discusses our methodology – the model and simulations (Section 2.1), the zoom and full-box reconstruction (Section 2.2), the simulation output (Section 2.3), and analysis details (Section 2.4). In Section 3 we present the TNG-Cluster sample. Section 4 explores the properties of the gaseous ICM, while Section 5 considers the stellar and SMBH components. We summarize our findings in Section 6.

¹ www.tng-project.org/cluster

2. Simulations

2.1. The TNG model and simulations

The TNG100 and TNG300 volumes of the IllustrisTNG project (hereafter, TNG; Pillepich et al. 2018a; Nelson et al. 2018b; Naiman et al. 2018; Marinacci et al. 2018; Springel et al. 2018), together with the high-resolution TNG50 simulation (Nelson et al. 2019a; Pillepich et al. 2019), are a series of three large cosmological volumes, simulated with gravomagnetohydrodynamics (MHD) and incorporating a comprehensive model for galaxy formation physics (Weinberger et al. 2017; Pillepich et al. 2018b).

The largest volume, TNG300, includes 2×2500^3 resolution elements in a ~ 300 Mpc box, giving it a baryon mass resolution of $1.1 \times 10^7 M_\odot$. The gravitational softening lengths are 1.5 kpc at $z = 0$ for the stars and dark matter, while gas cells have an adaptive gravitational softening with a minimum of 370 comoving pc (see Table 1). Adopting the fiducial TNG model, we extend this effort with our new project **TNG-Cluster**, which improves the statistics and sampling of the most massive dark matter halos, with total mass exceeding $\log(M_{200c}/M_\odot) > 14.5$ at redshift zero.

All aspects of the physical model, including parameter values and the simulation code, are described in Weinberger et al. (2017) and Pillepich et al. (2018b) and are kept unchanged for the TNG-Cluster simulation. In particular, TNG uses the AREPO code (Springel 2010), which solves for the coupled evolution under self-gravity and ideal, continuum MHD (Pakmor et al. 2011; Pakmor & Springel 2013). Self-gravity is solved with a Tree-PM approach, whereas the fluid dynamics use a Godunov type finite-volume scheme on an unstructured, moving, Voronoi tessellation. The numerical scheme is second order accurate in both time and space (Pakmor et al. 2016).

The simulations include a physical model for the most important processes relevant for the formation and evolution of galaxies. Specifically: (i) gas radiative processes, including primordial/metal-line cooling and heating from the background radiation field, (ii) star formation (SF) in the dense interstellar medium (ISM), (iii) stellar population evolution and chemical enrichment following supernovae Ia, II, as well as AGB stars, with individual accounting for the nine elements H, He, C, N, O, Ne, Mg, Si, and Fe, (iv) supernova driven galactic-scale outflows or winds (see Pillepich et al. 2018b, for details), (v) the formation, coalescence, and growth of SMBHs, (vi) and dual-mode SMBH feedback operating in a thermal ‘quasar’ state at high accretion rates and a kinetic ‘wind’ state at low accretion rates (see Weinberger et al. 2017, for details).²

We make one addition: coupling the Monte Carlo tracer particle population (Genel et al. 2013) to an active, on-the-fly shock finder (Schaal & Springel 2015) such that accretion properties including temperature, density, and shock mach number history are stored for every tracer (following Nelson et al. 2013). This change is entirely passive, and only provides new and previously unavailable information that can be used in future analyses.

One of the most important differences between the TNG-Cluster sample and other hydrodynamical simulations of galaxy clusters is its resolution and statistics. The TNG model for baryonic and feedback physics is also physically comprehensive, robust, and well-validated. In particular, the TNG model has been shown to produce realistic galaxy populations, consistent with

² TNG-Cluster adopts the same modification to the SF time-scale law as in TNG50, whereby gas cells with extremely short SF time-scales, in the densest environments, are converted into stars in a reasonable number of numerical time-steps (see Section 2.2 of Nelson et al. 2019a).

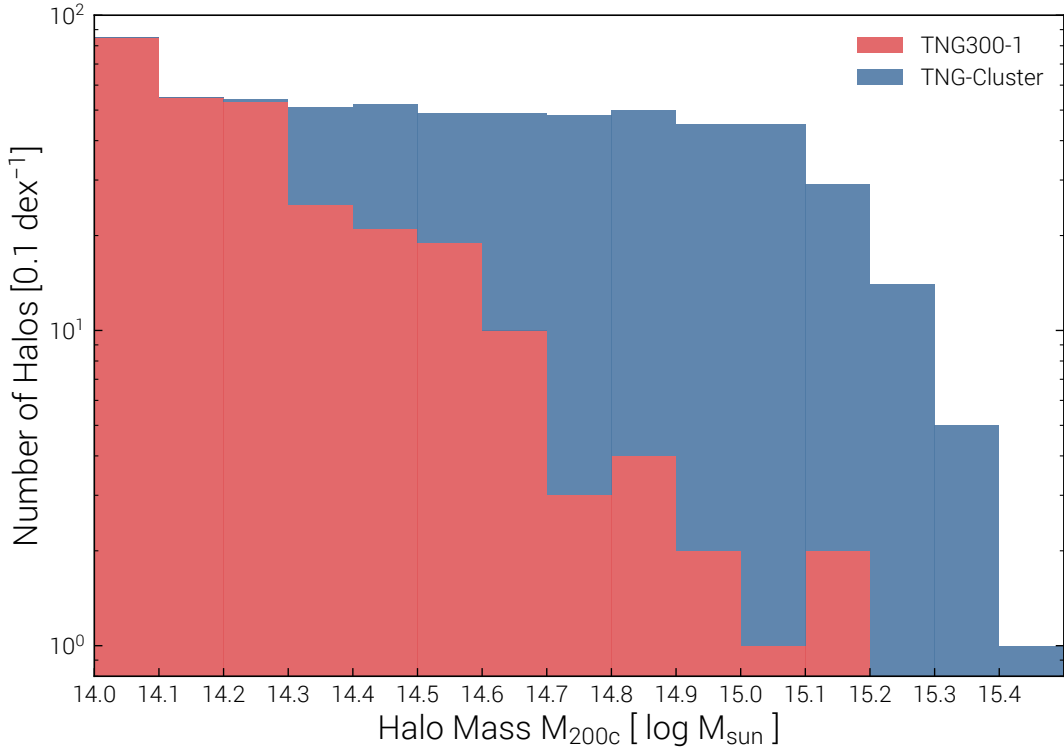


Fig. 1. The $z = 0$ cluster mass function of the new TNG-Cluster simulation project (blue) stacked on top of our existing cluster sample from TNG300 (orange), showing the number of halos per 0.1 dex bin in M_{200c} . We increase the statistics for halos $\gtrsim 10^{14.5} M_\odot$ by an order of magnitude, from ~ 30 objects to ~ 350 . Likewise, we increase the sampling of the most massive and rare $\gtrsim 10^{15} M_\odot$ halos by a factor of *thirty*, from just three halos in TNG300 to ninety in TNG-Cluster. The combined $M_{200c} > 10^{14} M_\odot$ cluster sample increases from 280 to 636 halos.

a broad range of observational constraints, across an enormous dynamic range, from small dwarf galaxies ($M_\star \simeq 10^8 M_\odot$) to massive galaxy clusters ($M_{\text{halo}} \simeq 10^{15} M_\odot$). For example, in the cluster regime, the TNG model has been validated in the cool-core/non-cool-core dichotomy (Barnes et al. 2018), ICM metallicity profiles (Vogelsberger et al. 2018), X-ray properties (Truong et al. 2020), satellite populations (Stevens et al. 2019, 2021; Donnari et al. 2020a,b; Ayromlou et al. 2021b), the colors (Nelson et al. 2018b), quenching (Donnari et al. 2019), and density structure (Wang et al. 2018b) of central early-types, their stellar halos (Pulsoni et al. 2020), lensing signals (Renneby et al. 2020) and Sunyaev-Zeldovich effect (Lim et al. 2021). As a result, the TNG-Cluster halos are simulated with a model that has a high degree of physical fidelity, for the thermodynamical properties of the ICM as well as the galaxy populations hosted therein. It is also the only cosmological simulation suite of massive clusters and their galaxies that self-consistently includes magnetic fields.

The TNG model is not perfect. Informative tensions and disagreements between previous IllustrisTNG simulations and observational data are discussed in the TNG public data release (Nelson et al. 2019b). As with all cosmological hydrodynamical simulations, the multi-scale, multi-physics nature of the physical phenomena involved require significant modeling approximations and uncertainties. At the cluster mass-scale, as an illustrative example, the TNG model does not include the relativistic jets launched from SMBHs, nor the non-thermal impact of cosmic rays. The use and interpretation of TNG-Cluster will benefit from careful comparisons with observations, a process we start here.

As in all TNG simulations, we adopt a Planck Collaboration (2016) cosmology with $\Omega_{\Lambda,0} = 0.6911$, $\Omega_{m,0} = 0.3089$, $\Omega_{b,0} = 0.0486$, $\sigma_8 = 0.8159$, $n_s = 0.9667$ and $h = 0.6774$.

2.2. Re-simulation and full volume reconstruction

TNG-Cluster is a suite of several hundred multi-mass ‘zoom’ re-simulations of cluster halos. To construct the initial conditions we first generate a random parent volume with $L_{\text{box}} = 1 \text{ Gpc}$ and $N_{\text{DM}} = 2048^3$, giving a particle mass of $m_{\text{DM}} \simeq 4 \times 10^9 M_\odot$. We run a gravity only version of this parent simulation, TNG-Cluster-Dark, which has more than sufficient resolution to accurately identify massive clusters. We choose target halos by selecting on $z = 0$ halo mass alone, making the sample unbiased in all other properties. The 352 halos are chosen randomly in 0.1 dex mass bins such that we (i) include all halos in the TNG-Cluster-Dark volume above $M_{200c} \geq 10^{15} M_\odot$, and (ii) compensate the drop-off of statistics in TNG300 from $10^{14.3}$ to $10^{15.0}$ to produce a flat distribution in halo mass over this range: see Figure 1.

For each target halo, we then select all member dark matter particles in its friends-of-friends group at $z = 0$ and trace them back to their coordinates in the initial conditions (at $z = 127$). We define this Lagrangian volume by constructing an adaptive oct-tree from $2^6 = 64$ up to $2^{11} = 2048$ grid cells per linear dimension, marking those cells that contain member particles. We then expand this marked region at the highest refinement level by progressively including neighboring cells until the total volume reaches three times its original value. This protects against contamination of the high-resolution region by low-resolution (i.e. high-mass) particles/cells at late times. The highest resolution grid is then refined by a further factor of four in linear extent, producing cells with 4^3 times smaller volume (lower mass). A particle set is created, with one total mass particle in each occupied cell – eight discrete mass levels, progressively coarsening away from the region of interest.

Table 1. Details of the TNG-Cluster simulation in comparison to its smaller volume siblings. The values are: volume, box side-length, number of initial gas cells, dark matter particles, and tracers; the mean baryonic cell mass and dark matter particle mass; the gravitational softening length minimum for the gas, and the softening for the collisionless components at $z = 0$; the number of groups ($\log M_{200c}/M_\odot$ from 13.0 to 14.0), lower mass clusters (14.0–14.5), intermediate-mass (14.5–15.0), and high mass (> 15.0) clusters. \dagger = effective full-volume equivalent. The TNG-Cluster numbers refer exclusively to the primary halos targeted for re-simulation.

Run		TNG50	TNG100	TNG300	TNG-Cluster
Volume	[Mpc ³]	51.7 ³	110.7 ³	302.6 ³	1003.8³
L_{box}	[Mpc/h]	35	75	205	680
N_{GAS}	-	2160 ³	1820 ³	2500 ³	8192^{3\dagger}
N_{DM}	-	2160 ³	1820 ³	2500 ³	8192^{3\dagger}
N_{TR}	-	2160 ³	2×1820^3	2500 ³	8192^{3\dagger}
m_{baryon}	[M _⊕]	8.5×10^4	1.4×10^6	1.1×10^7	1.2×10^7
m_{DM}	[M _⊕]	4.5×10^5	7.5×10^6	5.9×10^7	6.1×10^7
$\epsilon_{\text{gas,min}}$	[pc]	74	185	370	370
$\epsilon_{\text{DM,stars}}$	[pc]	288	740	1480	1480
N_{groups}	$10^{13.0-14.0}$	23	168	3,545	0
N_{clusters}	$10^{14.0-14.5}$	1	11	239	57
N_{clusters}	$10^{14.5-15.0}$	0	3	38	207
N_{clusters}	$> 10^{15.0}$	0	0	3	92

This particle set is then perturbed following the Zel'Dovich (1970) approximation to imprint our chosen transfer function, using the same procedure as for the original TNG uniform mass simulation initial conditions (Pillepich et al. 2018b) and the N-GENIC code (Springel et al. 2005), keeping the noise field consistent in the low-resolution grids and only adding additional small-scale power in the ‘zoom’ region (we assess the size of these zoom regions, and the level of low-resolution ‘contamination’, in Appendix A). The high-resolution volume has a spatial (mass) resolution that is 4 (64) times better than the original parent simulation, resulting in an effective resolution of $\sim 8192^3$, had the original volume been entirely covered by high resolution. This is in practice equivalent to TNG300-1, thereby extending the TNG300-1 cluster sample at roughly the same resolution.

With several hundred such multi-mass zoom simulations run to completion, we then reconstruct the parent volume at full resolution and with the hydrodynamical results, by stitching together the results of the individual zoom simulations. To do so we create the 100 saved snapshots and group catalogs (same configuration as TNG) by shifting the spatial coordinates of the box centered zooms to the correct position within the parent volume, offsetting particle IDs to maintain global uniqueness, converting the simulations back to the fiducial TNG unit system, and writing a file-level structure that enables the recovery of the exact particle set and/or group catalog of any of the original zooms. This reconstruction is ultimately for convenience: we label the resulting simulation **TNG-Cluster**. This ‘virtual box’ has an identical data structure to all other full volume TNG simulations to date, enabling seamless analysis and the application of all existing tools, codes, and post-processing pipelines.

Figure 2 visualizes our reconstruction of the TNG-Cluster volume from the series of independent zoom simulations. The total number of high resolution dark matter particles in TNG-Cluster is $\sim 2480^3$, making data storage and analysis expense roughly the same as for TNG300-1 ($N_{\text{DM}} = 2500^3$).

2.3. Simulation output and analysis

The output data of TNG-Cluster is identical to that of the previous TNG simulations, for both halo and galaxy catalogs and particle-level snapshots, with a few additions.

In particular, dark matter halos and galaxies in TNG-Cluster are identified as in all the TNG simulations, with a two-step process. First, the friends-of-friends algorithm (Davis et al. 1985) identifies associations of dark matter particles. Then, the SUBFIND algorithm (Springel et al. 2001) is applied to each halo in order to locate and characterize gravitationally-bound subhalos. Galaxies are subhalos containing non-zero stellar mass. Subhalos are tracked through time using the SubLink merger trees (Rodriguez-Gomez et al. 2015).

Data is stored at 100 snapshots between $z = 15$ and $z = 0$, with 20 full and 80 mini snapshots (Nelson et al. 2019b). In addition to all quantities from the previous TNG simulations, we also store additional fields for tracer particles (see Section 2). We also record details of the feedback energetics of each SMBH along their main evolutionary branches, as well as the timings and properties of the kinetic wind ejections from each SMBH.

When presenting results as a function of galaxy stellar mass, we define this quantity as the total stellar mass within a 3D spherical aperture of 30 pkpc. We also present results as a function of both M_{200c} and M_{500c} , which are the total halo masses within R_{200c} and R_{500c} , respectively. Both are defined as the radius within which the average mass density is 200 (500) times the critical density.

2.4. Observables

From the simulation outputs, we calculate several observables. For X-ray emission we compute broadband luminosities, typically 0.5 – 2.0 keV, using the collisional ionization tables of AtomDB from the Astrophysical Plasma Emission Code (APEC v3.0.9-201t; Smith et al. 2001). We derive the X-ray emissivity of each gas cell based on its density, temperature, and metallicity,

Introducing the TNG-Cluster Simulation

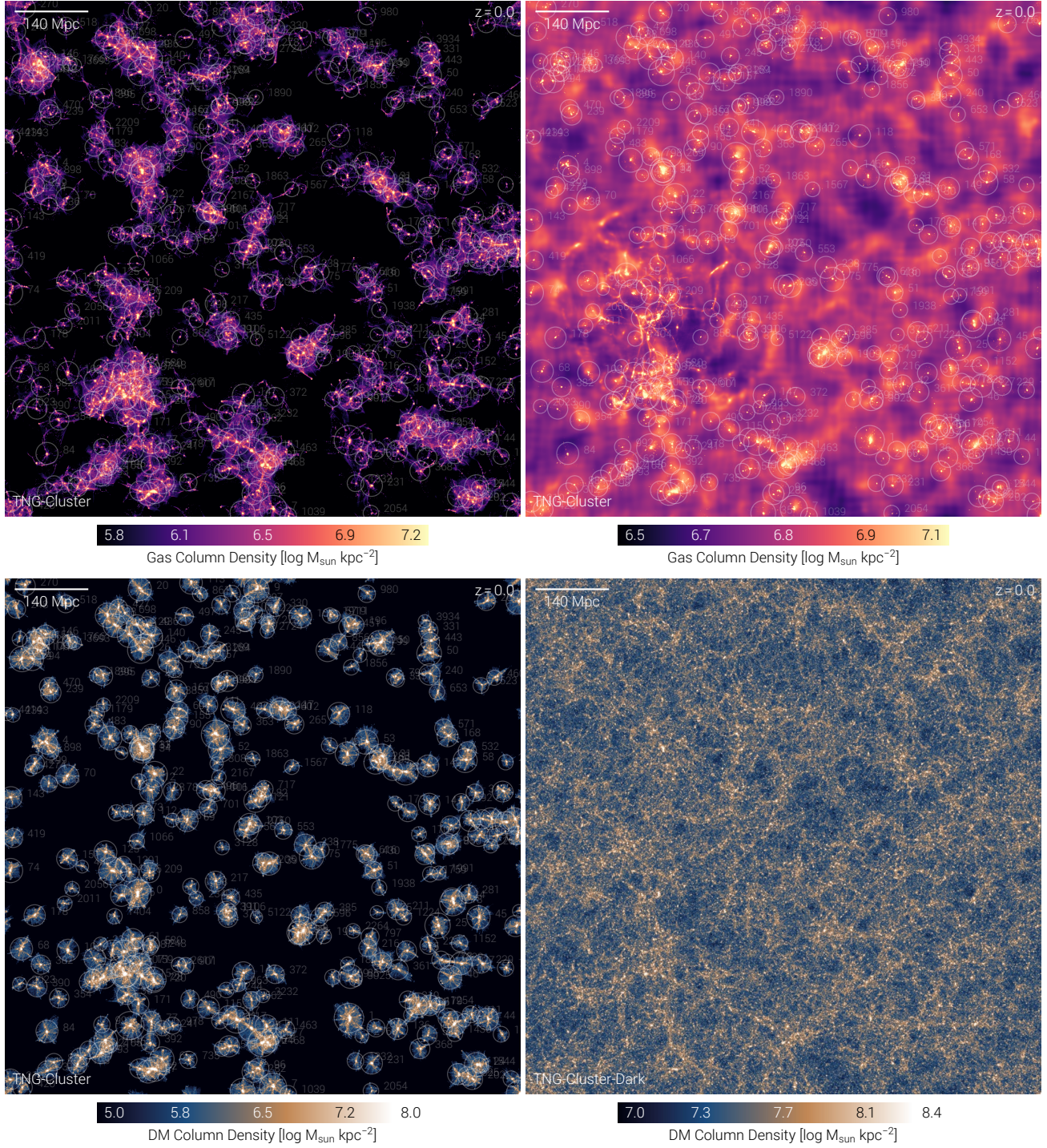


Fig. 2. Four visualizations of the TNG-Cluster volume at $z = 0$. TNG-Cluster is a ‘virtual’ simulation box constructed by stitching together the results of 352 individual zoom simulations. Each halo targeted for high-resolution simulation is marked by its Halo ID and a white circle demarcating $10r_{\text{vir}}$. **Top left:** projected gas column density, showing high-resolution gas together with the first three intermediate/buffer regions. **Top right:** FoF-scope gas of all halos (which exist only in high resolution regions), together with all outer fuzz of the first (most massive) zoom target, which evidences the gradual coarsening of resolution as we move away from the central re-simulated halos. **Lower left:** high-resolution dark matter particles. The visible areas of nonzero mass density therefore show exactly the high-resolution regions of the zooms. **Lower right:** the parent, gravity-only volume of TNG-Cluster-Dark, from which massive halos were chosen for re-simulation. Shown in projected dark matter surface density, the large-scale structure is consistent with the three other views from the reconstructed, hydrodynamical TNG-Cluster volume.

adopting the default [Anders & Grevesse \(1989\)](#) abundances. We label C, N, O, Ne, Mg, Al, Si, S, Ar, Ca, Fe, and Ni as metals and do not include other trace elements beyond H and He into this category (e.g. versus SOXS; [Zuhone et al. 2023](#)). For the high-temperature ICM plasma of our simulated clusters, there

is negligible difference versus a simpler calculation of free-free (bremsstrahlung) emission alone (e.g. [Navarro et al. 1995](#)).

As a proxy for the thermal Sunyaev-Zeldovich signal ([Sunyaev & Zeldovich 1970](#)), we compute the Compton y -parameter

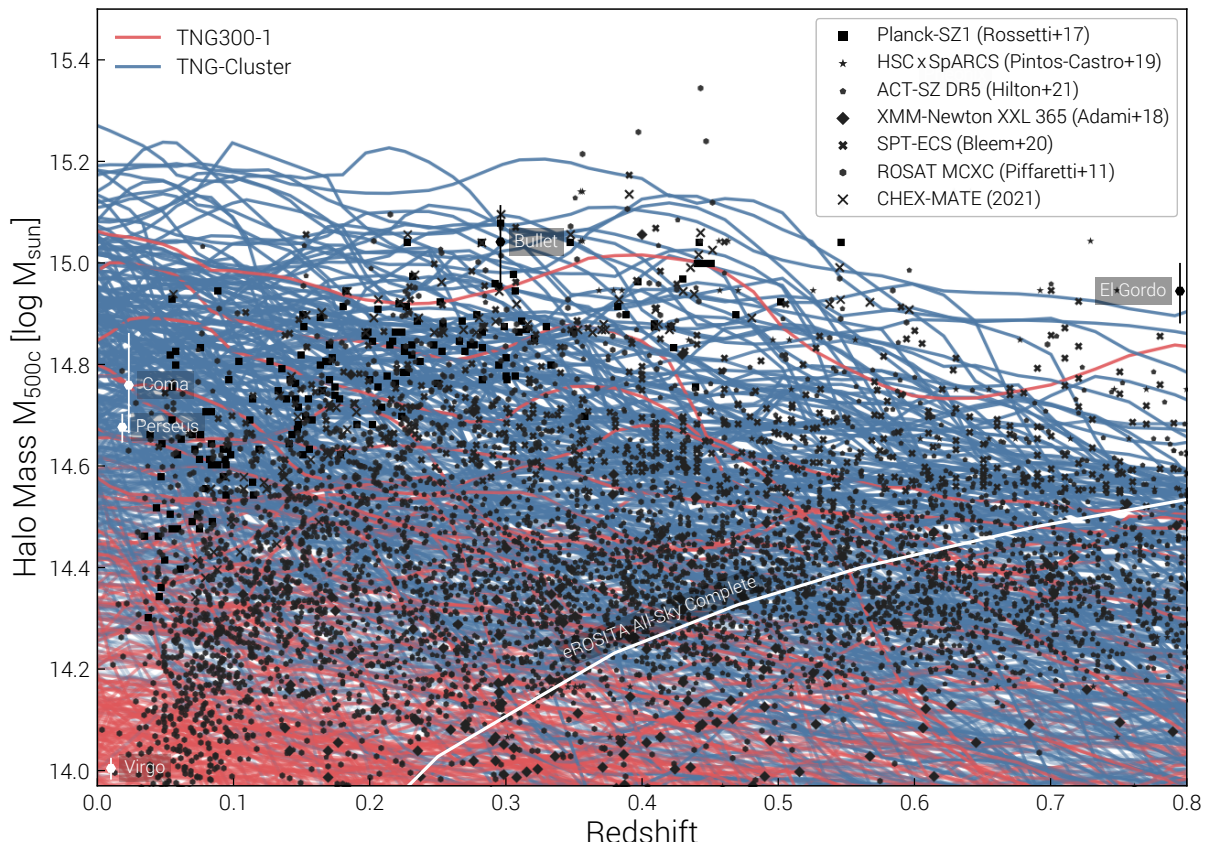


Fig. 3. The combined sample of TNG-Cluster (blue) and TNG300 (red), showing M_{500c} halo mass as a function of redshift. The mass assembly history of each $z = 0$ cluster is shown as a single line. For reference, we compare to observational samples of galaxy clusters from large surveys/survey instruments including Planck, ACT, ROSAT, SPT (black markers; see text for details). Several notable low-redshift named clusters are also included for comparison in this mass-redshift plane – Virgo, Coma, Perseus, the Bullet Cluster, and El Gordo (points with errorbars; see text for details). The TNG-Cluster sample, in blue, is essential to compare to the most massive detected galaxy clusters, from $z = 0$ to cosmic noon.

$$y = \int \sigma_T \frac{k_B T}{m_e c^2} n_e dl \propto \int P_e dl \quad (1)$$

which is dimensionless, and proportional to the line-of-sight integral (dl) of electron pressure. Here σ_T is the Thomson cross-section, k_B is Boltzmann's constant, T is gas temperature, m_e is the mass of the electron, c is the speed of light, and n_e is electron number density. In practice, to compute y we calculate and sum $Y = \sigma_T (k_B T) / (m_e c^2) \times m / (\mu_e m_H)$ for gas cells, where m is the total gas cell mass, μ_e is the mean molecular weight per free electron, and m_H is the atomic mass of the hydrogen atom (following Roncarelli et al. 2007; Kay et al. 2012; McCarthy et al. 2014).

We typically consider X-ray luminosities and integrated Y_{SZ} parameters integrated within spherical 3D apertures of R_{500c} , in which case contributions from all gas cells are summed directly. When measuring instead in 2D projection, or creating maps of X-ray emission or SZ signal, we adopt the usual cubic-spline kernel projection approach (following Nelson et al. 2016) with a line-of-sight projection depth equal to the (cosmologically large) full box depth, thereby including reasonable 2-halo contributions as well as projection effects.

In both cases star-forming gas, which is pressurized by our two-phase sub-grid model, is assigned its cold phase temperature of 1000 K, and so does not contribute to X-ray or SZ signals.

We also make a simple computation of the radio synchrotron emission from our simulated clusters (following Xu et al. 2012;

Marinacci et al. 2018). We track the evolving magnetic energy in each gas cell, but do not directly follow relativistic particles. We therefore assume a relativistic electron population following a power-law in number density per energy bin $dn(\gamma)/d\gamma \propto \gamma^{-p}$ where γ is the Lorentz factor and $p = 1.7$ is the spectral index. We further assume that only electrons between $\gamma_{\min} = 300$ to $\gamma_{\max} = 1.5 \times 10^4$ contribute, that the energy density ratio between relativistic protons and electrons is $k = 10$ (Vazza & Brüggen 2014), and that the total energy density in relativistic particles (electrons plus protons) is a ratio $\eta = 1$ of the magnetic energy density, i.e. equipartition, as inferred to be the case for galaxy clusters (Pinzke & Pfrommer 2010). The resulting synchrotron power is derived for a VLA-like configuration with a central frequency of 1400 MHz and a bandpass of 20 MHz (see appendices A1 and A2 of Marinacci et al. 2018). The radio synchrotron emission of TNG-Cluster is explored in more detail, and with more sophisticated modeling, in (Lee et al. 2023).

3. The TNG-Cluster Sample

In Figure 1 we show the combined cluster mass functions of TNG300 (in red) and TNG-Cluster (in blue) at redshift zero. The TNG-Cluster simulation samples tens of objects more massive than even the most massive cluster present in TNG300, with halo mass $M_{200c} > 10^{15.2} M_\odot$. For massive clusters with total mass $M_{200c} > 10^{15.0} M_\odot$, TNG-Cluster improves upon the statistics of TNG300 by a factor of thirty, increasing the sample from just

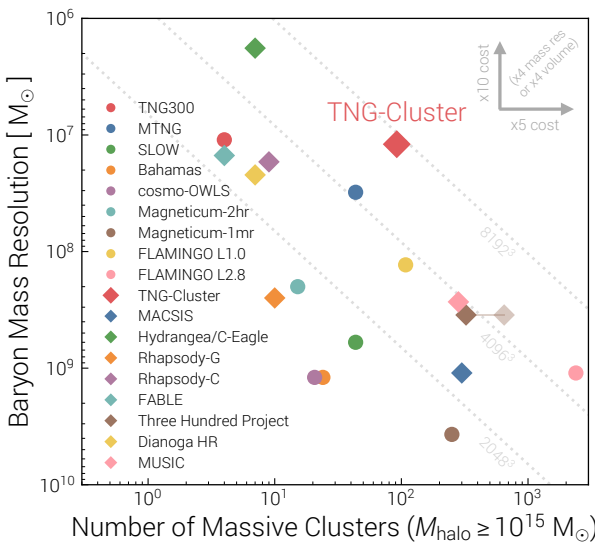


Fig. 4. Comparison of the TNG-Cluster sample, introduced here, to other simulated cluster ensembles. For each simulation we contrast the numerical resolution, in terms of gas/baryonic mass resolution (y-axis), versus the number of simulated massive halos with $M_{200c} \geq 10^{15} M_\odot$ (x-axis). We include only cosmological hydrodynamical simulations of galaxies, both uniform boxes (circles) and zoom-in suites (diamonds). The vast majority of these simulations include models for both stellar and supermassive black hole feedback physics, although they vary in many key aspects (see text for details).

three objects to ninety. Likewise, for intermediate mass halos with $M_{200c} > 10^{14.5} M_\odot$, we boost the number of simulated clusters by one order of magnitude, from ~ 30 halos to ~ 300 . Ultimately we compensate the drop-off of the TNG300 mass function starting at $10^{14.3} M_\odot$, sampling to achieve a roughly flat log mass spectrum until $10^{15.0} M_\odot$, where we let the statistics of a 1 Gpc volume limit the sample. All halos above $10^{15.0} M_\odot$ total mass are resimulated, providing a complete volume-limited sample of the highest-mass clusters: the exact numbers are given in Table 1.

Figure 3 gives an overview of the simulated cluster sample available in TNG-Cluster, in comparison to several observational samples and as a function of redshift. We compare to the following large surveys: a subset of 169 clusters from the Planck SZ-selected (PSZ1-cosmo) catalog with X-ray followup (Rossetti et al. 2017); the ACT DR5 SZ-selected cluster sample (Hilton et al. 2020); the ROSAT MCXC meta-catalog (Piffaretti et al. 2011); the SPTpol extended cluster survey (SPT-ECS; Bleem et al. 2020); the XMM-Newton based XXL 365 cluster catalog (Adami et al. 2018); and the PSZ2-selected CHEX-MATE cluster sample (CHEX-MATE Collaboration et al. 2021). We also show the Coma cluster at $M_{500c} = 5.7^{+1.5}_{-1.1} \times 10^{14} M_\odot$ (Okabe et al. 2014), the Perseus cluster at $M_{500c} = 4.7^{+0.3}_{-0.3} \times 10^{14} M_\odot$ (Simionescu et al. 2011), the Virgo cluster at $z = 0$ and $M_{500c} = 0.8^{+0.1}_{-0.1} \times 10^{14} M_\odot$ (moved slightly in mass for visibility; Simionescu et al. 2017), the Bullet Cluster at $z = 0.296$ with $M_{500c} = 1.1^{+0.2}_{-0.2} \times 10^{15} M_\odot$ (Clowe et al. 2006), the Phoenix cluster at $z = 0.6$ and $M_{500c} = 2.3^{+0.7}_{-0.7} \times 10^{15} M_\odot$ (Tozzi et al. 2015), the El Gordo cluster with $M_{500c} = 8.8^{+1.2}_{-1.2} \times 10^{14} M_\odot$ (moved from $z = 0.87$ to $z = 0.8$ for visibility; Botteon et al. 2016), and the eROSITA threshold mass above which every halo on the sky will be X-ray detected (Pillepich et al. 2012; Merloni et al. 2012). Figure 3 demonstrates that TNG-Cluster well samples the mass-redshift space of recent observed cluster samples.

In order to compare to other samples of simulated clusters, Figure 4 shows TNG-Cluster in terms of the volume versus resolution compromise: on the plane of baryonic mass resolution (better upwards) against the number of simulated massive clusters. We define massive clusters as having $M_{\text{halo},200c} > 10^{15} M_\odot$ and only include cosmological (non-idealized) hydrodynamical (with gas) simulations run to $z = 0$. Filled circles represent uniform volume (i.e. ‘full box’) cosmological simulations, while diamonds represent suites of zoom-in cluster halos.

TNG-Cluster occupies a unique region of this parameter space, and even more so with the joint TNG300 plus TNG-Cluster sample. In terms of statistics, it is most similar to The Three Hundred cluster simulation project (Cui et al. 2018, 2022), albeit with only one physical model realised, but with 100 times improved mass resolution. The Hydrangea/C-EAGLE simulations (Bahé et al. 2017; Barnes et al. 2017a) provide much smaller samples, albeit at higher TNG100-like resolution. The MACSIS sample (Barnes et al. 2017b) as well as large hydrodynamical boxes, particularly cosmo-OWLS (Le Brun et al. 2014), BAHAMAS (McCarthy et al. 2017), and Magneticum (Dolag et al. 2016) also provide comparable, to far larger, samples, but at mass resolutions orders of magnitude worse than TNG-Cluster. This is also the case for the original MUSIC sample (Sembolini et al. 2013) and Omega500 NR (Nelson et al. 2014), although these simulations contain much simpler physics, i.e. without AGN feedback and/or without broad empirical calibration on basic observables such as gas fractions. The recent MillenniumTNG (Pakmor et al. 2023b) and FLAMINGO (Schaye et al. 2023) large-volume simulations include similar (to much larger) cluster samples at similar (to much worse) resolution. Much smaller samples with comprehensive/validated physical models include the DIANOGA simulations (Bassini et al. 2020) and the FABLE cluster zooms (Henden et al. 2018). Finally, the original Rhapsody-G clusters (Hahn et al. 2017) have been updated with more sophisticated physics, including AGN dynamics, feedback, and thermal conduction with Rhapsody-C (Pellissier et al. 2023).³

Even with ‘basic’ galaxy formation physics, simulating high-mass galaxy clusters in the full cosmological context at high numerical resolution – i.e., that achievable at Milky Way halo-mass scales (e.g. Guedes et al. 2011; Grand et al. 2016; Pillepich et al. 2023; Wetzel et al. 2023), much less dwarf galaxy scales (e.g. Wang et al. 2015; Hopkins et al. 2018; Smith et al. 2019; Agertz et al. 2020) – is impossible. Clusters simply contain so much mass that resolving these structures at high resolution is computationally demanding. In this context, TNG-Cluster strikes a balance between detail and statistics. It remains at a baryon mass resolution of $\sim 10^7 M_\odot$ (equivalent to TNG300-1), which although low in the context of the IllustrisTNG model and simulations, is high in the context of other cluster simulations. As a result, it is able to include a population of ~ 100 clusters with $M_{200c} \geq 10^{15} M_\odot$, enabling unbiased and population-wide comparisons and results. A selection of key physical properties of the main systems simulated within TNG-Cluster are given in Table B.1.

Throughout this paper, we exclusively focus on the 352 systems that are the primary zoom targets of the simulation suite, namely the most massive halos in the zoom regions at $z = 0$ and their progenitors. In addition to those halos, TNG-Cluster contains many ‘bonus’ halos at high (i.e. uncontaminated) resolution. In particular, there are 241 (9110) additional group (Milky Way)

³ TNG50 and TNG100, as well as the original Illustris simulation, EAGLE, and SIMBA all contain no, to $O(1)$, high-mass clusters, and we exclude them here. We also exclude YZiCS (Choi & Yi 2017), nIFTy (Sembolini et al. 2016), and ISC (Vazza et al. 2017), which contain zero or one such clusters.

mass halos with $M_{200c} \geq 10^{13}$ (10^{12}) M_\odot , i.e. TNG-Cluster also contains large populations of nearby halos in the high density environments centered on clusters.

4. Properties of the Intracluster Medium Gas

4.1. Visual Overview

We begin to explore the richness and detail of the TNG-Cluster results by visualizing a number of spatially resolved physical properties and observable quantities of a single halo.

Figure 5 shows seven projections for the third most massive cluster at $z = 0$, with a total halo mass of $M_{200c} \simeq 10^{15.2} M_\odot$. The main panel focuses on a key observable of galaxy clusters: X-ray emission from the ICM. We show the soft-band (0.5 – 2 keV) X-ray surface brightness on the scale of the virial radius (white circle). While centrally concentrated, we also see: (i) a bright merger front feature to the lower left of the core (Zhang et al. 2020a), (ii) a filamentary bridge of extended emission extending off to the left (Reiprich et al. 2021), (iii) two infalling substructures and early sloshing fronts just outside R_{200c} (ZuHone et al. 2011), and (iv) small-scale, wispy, filamentary, and tail-like features throughout the ICM, signposts of lower mass accreting satellites, gas stripping, and jellyfish galaxies (Yun et al. 2019).

The smaller six panels below show, from left to right: dark matter projected density, stellar mass density, the Sunyaev-Zeldovich Compton-y map, gas-phase metallicity, magnetic field strength, and cool gas as traced by neutral hydrogen column density. All are shown on the same scale as the main panel.

The distribution of dark matter (middle left panel) reveals the substructure richness of massive clusters (Angulo et al. 2012). In TNG-Cluster, this single halo is resolved with $\sim 100,000,000$ particles/cells, and contains a total of 19,700 resolved subhalos, with total masses between $8.2 < M_{\text{sub}}/M_\odot < 14.6$, of which 3,500 are luminous galaxies with stellar masses spanning $6.8 < M_{\text{sub},\star}/M_\odot < 12.6$. The spatial distribution of these stars (middle center panel) reveals the massive central galaxy (i.e. BCG), a large satellite population, and the diffuse intracluster light (Lin & Mohr 2004; Conroy et al. 2007; Pillepich et al. 2018a).

These two collisionless components assemble within the gaseous component. In addition to X-ray emission, this hot plasma of the ICM of clusters is also commonly observed via the Sunyaev-Zeldovich effect, whereby cosmic microwave background photons interact with free electrons via inverse Compton scattering (Sunyaev & Zeldovich 1970). The resulting spectral distortions include thermal, kinetic, and polarization signatures – all are modulated by the impact of galaxy formation i.e. feedback physics (Nagai 2006). We show the dimensionless Compton y-parameter map (middle right panel) as a measure of the thermal SZ effect (tSZ; see Section 2.3). The central cluster and the substructure to the lower right are both clearly visible, while the lower mass infaller to the upper left has a factor of 10 smaller integrated Y_{SZ} . The spatially resolved SZ maps are significantly smoother than for X-ray emission (Battaglia et al. 2012), that traces the same hot phase but with a stronger density dependence.

The SZ morphology is also significantly smoother than the distribution of gas-phase metals (lower left panel), which is inhomogeneous and clumpy throughout the cluster volume. The cluster core reaches metallicities of $\sim Z_\odot/2$. The bulk of the cluster ICM is also highly enriched, with a shallow gradient and still $\gtrsim 0.1Z_\odot$ out to the virial radius (Ettori et al. 2015; Yates et al. 2017; Mernier et al. 2017). This reflects an interplay between metal expulsion through feedback-driven outflows and

environmental pre-enrichment of subsequent accretion (Vogelsberger et al. 2018).

Magnetic fields in TNG-Cluster are self-consistently amplified from a vanishingly small primordial seed field in the initial conditions to their present day values due to a combination of turbulent and small-scale dynamo processes (Pakmor et al. 2014, 2017).⁴ In the dense cores of clusters, magnetic fields reach values of $\gtrsim 10\mu G$, rapidly decreasing with density and distance towards cluster outskirts (Marinacci et al. 2018). The resolved magnetic field structure hints to a turbulent and complex small-scale topology (Domínguez-Fernández et al. 2019), large-scale features associated with anisotropy of the ICM and feedback-driven outflows (Nelson et al. 2021; Ramesh et al. 2023a), and dynamical effects from satellite galaxy draping (Pfrommer & Jonathan Dursi 2010).

As satellites infall and begin to orbit within the ICM they are subject to strong environmental processes including ram-pressure stripping (Ayromlou et al. 2021a). The removal of their cold interstellar medium (ISM) gas is traced by the distribution of neutral hydrogen (Rohr et al. 2023b) throughout the cluster (lower right panel). Low column density gas ($12 \lesssim \log N_{\text{HI}} [\text{cm}^{-2}] \lesssim 17$) is present throughout the cluster. The central galaxy is itself devoid of any significant amount of cool gas, although this is not always true, as we discuss below. Lyman-limit systems (LLS; $N_{\text{HI}} > 10^{17} \text{ cm}^{-2}$, in green) and damped Lyman-alpha absorbers (DLA; $N_{\text{HI}} > 10^{20.3}$, in orange) are strongly localized around satellite galaxies. In some cases, extended tails of stripped gas produce ‘jellyfish’ phase galaxies (Poggianti et al. 2017; Zinger et al. 2023). In this final panel we also include smaller white circles marking the location and size of the 100 most massive subhalos of this cluster – while some contain abundant HI, others are entirely devoid of gas due to environmental effects which eventually quench the star formation of cluster member galaxies (Bahé & McCarthy 2015; Donnari et al. 2020b).

Although not atypical, this single cluster is not necessarily representative of the population, and its properties cannot showcase the full diversity of the TNG-Cluster sample. Figure 6 therefore shows a gallery of X-ray emission from the 72 most massive $z = 0$ halos in the simulation, with the same spatial scale, and color scale, as above. In every stamp, the white circle shows R_{200c} . Some clusters are clearly isolated, relaxed, non-merging systems. Their X-ray morphologies are to first order circularly symmetric and centrally peaked. However, a large fraction of clusters exhibit strongly perturbed X-ray surface brightness maps indicative of ongoing mergers (Poole et al. 2006; ZuHone et al. 2011). Many systems also exhibit three or more distinct X-ray components (Monteiro-Oliveira 2022), suggesting complex merger scenarios and potentially accretion along preferred, large-scale filament directions (Colberg et al. 2005; Kartaltepe et al. 2008).

4.2. Properties and Observables of the Hot ICM

4.2.1. Halo gas mass fraction

We begin our quantitatively exploration of the properties of TNG-Cluster with total halo gas content. Figure 7 shows the $z = 0$ halo-scale gas fractions ($M_{\text{gas},500}/M_{500c}$) as a function of halo mass. The cosmic baryon fraction $f_{\text{b,cosmic}} = \Omega_{\text{b}}/\Omega_{\text{m}} \simeq 0.16$ is indicated by the horizontal dotted line. Red and blue symbols show clusters from TNG300 and TNG-Cluster, respectively.

⁴ Magnetic field amplification with the AREPO ideal MHD solver has been well studied in the Auriga simulations (Pakmor et al. 2023a). B fields were omitted from MillenniumTNG due to memory constraints, making TNG-Cluster uniquely informative at the high-mass end.

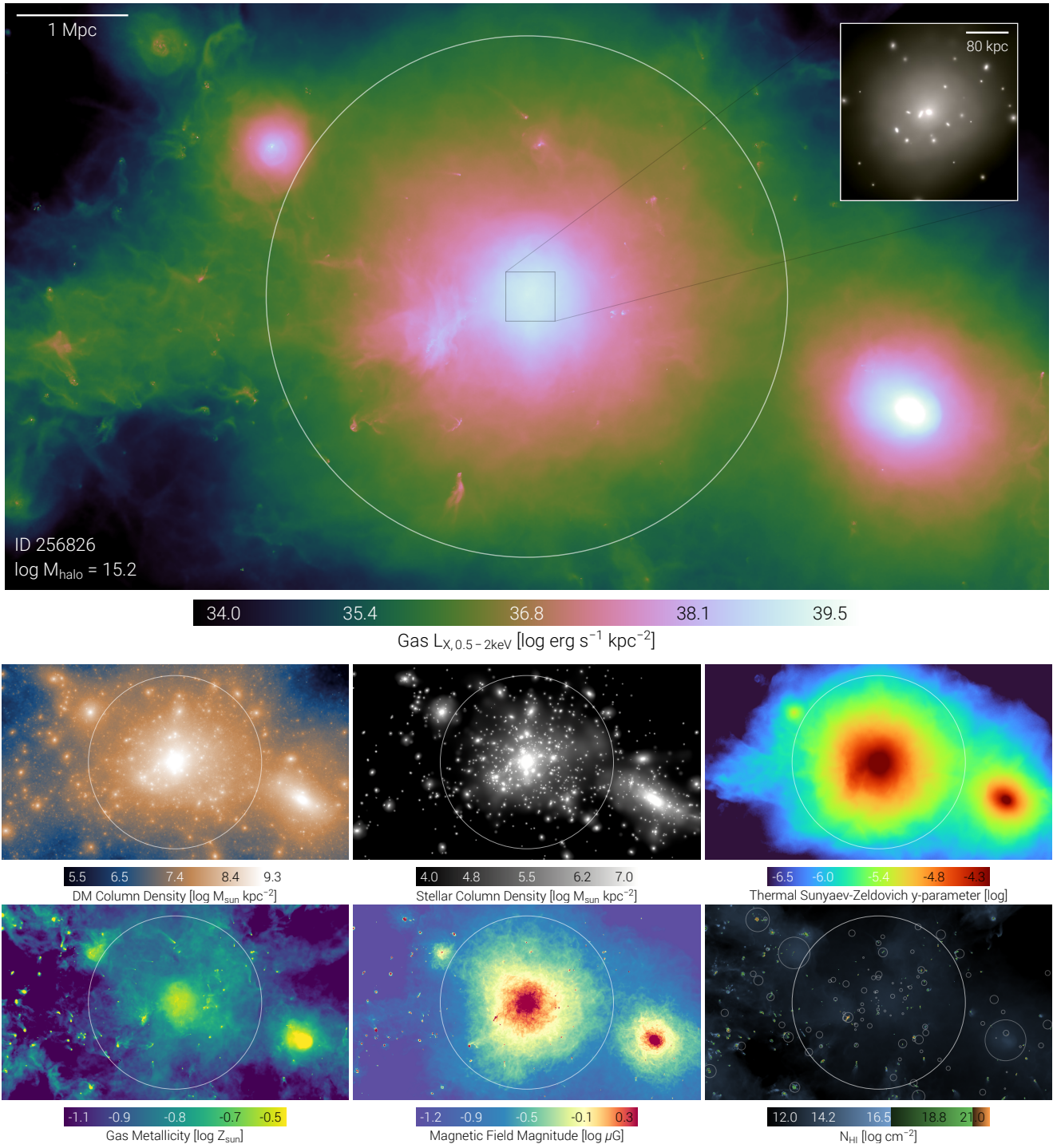


Fig. 5. Visualization of the gaseous, stellar, and dark matter distribution and physical properties for the third most massive halo in TNG-Cluster at $z = 0$, with a total mass $M_{200c} \approx 10^{15.2} M_{\odot}$. The main panel shows soft-band (0.5 – 2 keV) X-ray surface brightness, while the zoomed inset shows a mock stellar light image of the brightest central/cluster galaxy (BCG). The smaller panels show dark matter density, stellar density, the Sunyaev-Zeldovich y -parameter map, gas-phase metallicity, magnetic field strength, and neutral HI column density. In this final panel, the location and size of the 100 most massive subhalos are also indicated with circles. In all cases, the white circles mark R_{200c} . This single halo is resolved in TNG-Cluster with $\sim 100,000,000$ resolution elements, split between dark matter, stars, gas cells, and SMBHs. It contains $\sim 20,000$ resolved substructures, including $\sim 3,500$ luminous (satellite) galaxies. Not pictured: the cluster also hosts ~ 800 SMBHs with $M \geq 10^6 M_{\odot}$, and the central SMBH has a total mass of $\sim 10^{10.2} M_{\odot}$. Our [online TNG-Cluster ‘infinite galleries’](#) show similar projections across the full sample of 352 halos.

This figure extends towards higher masses a similar analysis of TNG100 and TNG300 by Pop et al. (2022). We include observational data derived from X-ray measurements (Giordini et al. 2009; Gonzalez et al. 2013; Lovisari et al. 2015, 2020), and kSZ extracted from Planck data (Tanimura et al. 2021). The TNG-Cluster

gas fractions are relatively flat across the cluster mass regime. Data agrees that massive clusters have high $f_{\text{gas},r500c} \gtrsim 90\%$ of the cosmic baryon fraction. However, at least some observations suggest stronger trends arising from smaller inferred f_{gas} at

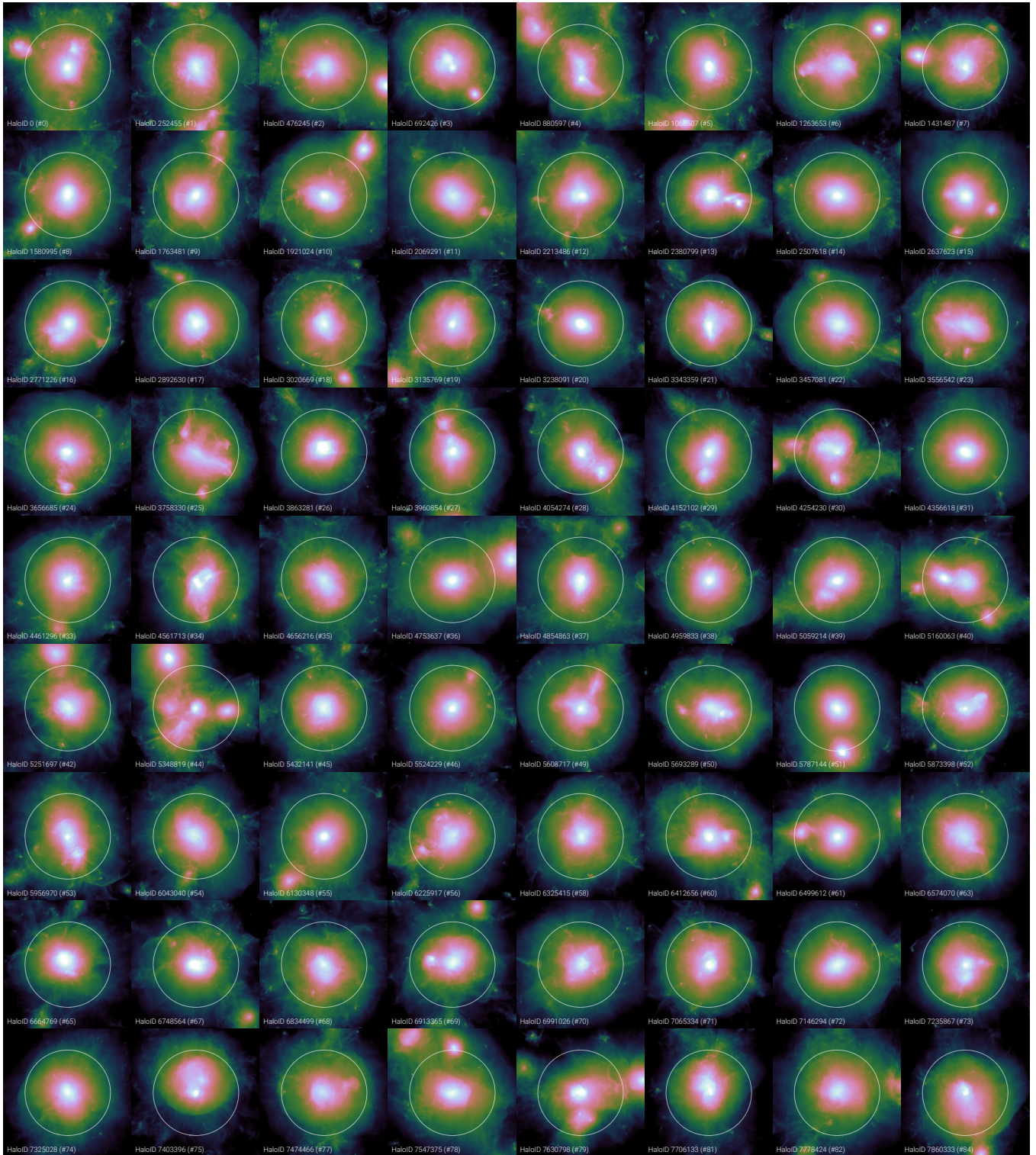


Fig. 6. Gallery of the first 72 halos of TNG-Cluster at $z = 0$, showing soft-band (0.5 – 2 keV) X-ray luminosity. The colormap is the same as Figure 5. Each panel is $2r_{\text{vir}}$ across, while the white circles mark r_{vir} , and halo IDs are labeled. A variety of X-ray morphologies are evident, from relaxed, centrally peaked surface brightness distributions, to un-relaxed and binary merging clusters, triple and multi-component merging systems, and large scale sloshing and gas displacement effects.

$M_{500c} \lesssim 10^{14.4} M_{\odot}$ (e.g. Chiu et al. 2018), suggesting that group gas fractions in TNG may be on the high side.

While the highest mass clusters are baryonically closed, with $f_b \simeq f_{b,\text{cosmic}}$ (Ayromlou et al. 2023a), this is not the case for low mass clusters and groups, where AGN feedback can significantly reduce the gas content of dark matter halos (McCarthy et al.

2011; Genel et al. 2014). Gas fractions (in group-mass halos) correlate well with the impact of baryons on the total matter power spectrum (on certain scales; van Daalen et al. 2011; Aricò et al. 2021; Giri & Schneider 2021), implying that realistic halo gas fractions are important for precision cosmology applications.

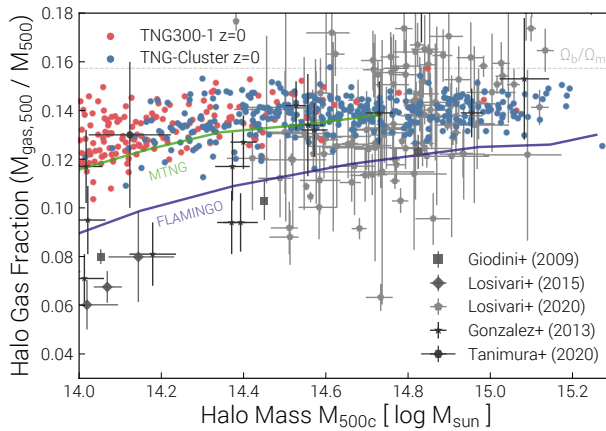


Fig. 7. The gas fraction of halos, taken as the ratio of gas mass to total mass, both within a 3D aperture of R_{500c} . We compare to observational inferences derived from X-ray emission (Giordini et al. 2009; Gonzalez et al. 2013; Lovisari et al. 2015, 2020), measurements of the kinetic Sunyaev-Zeldovich effect (Tanimura et al. 2021). In all three cases, in lieu of detailed mock observations enabling apples-to-apples evaluation, this is a qualitative, at face-value comparison only. For comparison, the green and purple solid curves are the running averages from the recent MTNG and FLAMINGO simulations.

Several caveats exist for our comparison with f_{gas} data. X-ray, weak lensing, and SZ-based estimates of gas content and/or total halo mass have different and non-negligible systematic uncertainties involved, and we emphasize that this comparison with data is meant to be qualitative, at face value, only. We have also not added observational uncertainty to the simulated points, such that (i) the simulated scatter is by definition smaller than the apparent observational scatter, and (ii) the simulated points are confined to $f_{\text{gas}} < f_{\text{b,cosmic}}$, which is not true for the data. Further, X-ray based inferences of halo-scale gas fractions rely on the assumption of hydrostatic equilibrium, which is not generally true (Rasia et al. 2006). Simulations suggest hydrostatic biases of $b \sim 0.1 - 0.3$ (Barnes et al. 2021; Jennings & Davé 2023). A comparison can approximately correct for this effect (Schaye et al. 2023), or forward model the X-ray emission to enable true apples-to-apples comparisons (Biffi et al. 2013). Leaving such detailed synthetic observations for the future, we broadly conclude that the TNG-Cluster gas fractions are qualitatively consistent with data, with quantitative agreement to be demonstrated.

We also compare to the recent FLAMINGO (purple line; Schaye et al. 2023) and MTNG (green line; Pakmor et al. 2023b) simulations. As expected, the MTNG gas fraction trend is compatible with TNG-Cluster, albeit without the high-mass end sampling. In contrast, FLAMINGO has noticeably $\sim 15\%$ lower $f_{\text{gas},r500c}$ in high-mass clusters, highlighting the impact of different baryonic feedback models even in these massive halos.

4.2.2. Magnetic field and synchrotron emission

Figure 8 shows a first look at the magnetic field properties of the ICM in TNG-Cluster (see also Marinacci et al. 2018, for a TNG300 analysis). For each halo we derive the mean, volume-weighted magnetic field strength within $0.5 R_{500c}$ at $z = 0, 1, 2$ and for all three redshifts show the trend with halo mass. Circular and square symbols show halos from TNG300 and TNG-Cluster, respectively. In the TNG model, the magnetic field strength in gaseous halos declines rapidly with increasing distance (Marinacci et al. 2018; Ramesh et al. 2023a,b), so values of $|B|$ in the

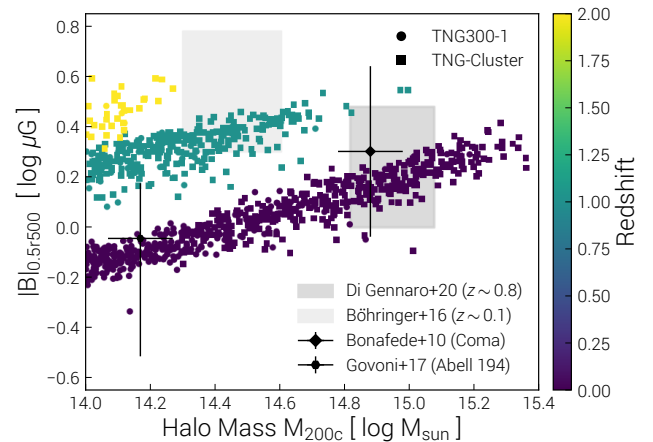


Fig. 8. The volume-weighted mean magnetic field strength in μG , measured for all gas within $0.5 R_{500c}$ of halos, as a function of halo mass. Color indicates three distinct redshifts considered, from $z = 0$ to $z = 2$. Circular (square) markers show halos from TNG300 (TNG-Cluster). We provide several qualitative, face-value comparisons with observational inferences from Faraday rotation measure analyses (Bonafede et al. 2010; Böhringer et al. 2016; Govoni et al. 2017; Di Gennaro et al. 2020). The magnetic field strength in the inner ICM has characteristic values of order $\sim \mu\text{G}$, increasing for larger halo masses, higher redshifts (at fixed mass), and smaller cluster-centric distances.

core (outskirts) of our simulated clusters are significantly higher (lower). This particular choice roughly approximates an average value over the inner ICM which could be inferred observationally.

We make several comparisons with data, which are meant in the qualitative sense only. For the Coma cluster, Faraday rotation measure (RM) modeling infers a decreasing magnetic field strength with halocentric distance, from $\sim 4\mu\text{G}$ to $\sim 1\mu\text{G}$ in the outskirts (Bonafede et al. 2010). For comparison we also include the lower mass Abell 194 cluster, where the uncertainty shows the difference between the central value of $\langle B_0 \rangle = 1.5\mu\text{G}$ and the ~ 1 Mpc halo volume average $B \sim 0.3\mu\text{G}$ (Govoni et al. 2017). Measurements of diffuse radio emission from clusters with LOFAR now infer that magnetic fields in intermediate redshift clusters $z \sim 0.7 - 0.8$ are similar to local clusters, with $B \gtrsim 1 - 3\mu\text{G}$, implying a relatively fast early amplification mechanism (dark gray; Di Gennaro et al. 2020). Measurements of RM place a similar constraint of $B \sim 2 - 6(l/10\text{kpc})^{-1/2}\mu\text{G}$ at $z \sim 0.1$, where l is the magnetic coherence length of the ICM (light gray; Böhringer et al. 2016). Given the limited observational statistics, different methodologies, and myriad physical assumptions for each method, data broadly infer cluster magnetic fields of $\sim \mu\text{G}$ with ~ 1 dex uncertainty (Carilli & Taylor 2002).

Given the magnetized ICM, Figure 9 presents a first look at the cluster radio synchrotron emission. An in-depth modeling effort for the diffuse radio emission in cluster outskirts, as accelerated by cluster merger shocks, and the diverse morphologies of radio relics in TNG-Cluster, is presented in a companion paper (Lehle et al. 2023).

Here we adopt a simple post-processing model to estimate the relativistic electron populations in each gas cell, and thus their observable emission, which is not directly tracked in the simulation (see Section 2.4). The resulting synchrotron power is a steep function of halo mass, rising from $P \sim 10^{22} \text{ W Hz}^{-1}$ for $M_{500c} = 10^{14} M_\odot$ to $P \sim 10^{25} \text{ W Hz}^{-1}$ by $M_{500c} = 10^{15} M_\odot$. Red and blue symbols show halos from TNG300 and TNG-Cluster, respectively. The clear mass trend is accompanied by a

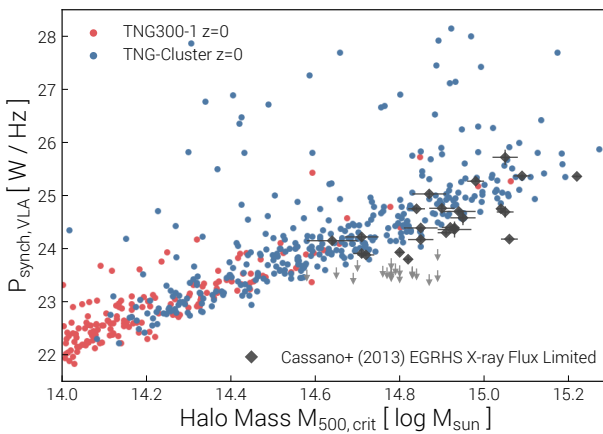


Fig. 9. Halo radio synchrotron emission. We show P_{synch} at 1.4 GHz for a VLA-like configuration, adopting a simple model for the relativistic electron population that assumes equipartition with the magnetic energy density (see text for details). Radio power rises rapidly with increasing halo mass, following an overall clear relation plus a small fraction of highly emitting outliers. Halo integrated synchrotron emission in TNG-Cluster is in the ballpark of observational results (Cassano et al. 2013).

small number of outliers which have, surprisingly, significantly enhanced synchrotron emission, by up to several orders of magnitude. We speculate that these may reflect ongoing mergers and strong gas compression events.

In gray symbols with error bars, and gray upper limits, we show results from the Extended GMRT Radio Halo Survey (EGRHS; Cassano et al. 2013). This is a sample of 67 deep pointed 1.4 GHz radio observations, based on X-ray flux limited selections with ROSAT. The detections scatter well within the region occupied by TNG-Cluster halos. At the same time, we have no simulated clusters at much lower values, which would be consistent with the upper limits of that sample. Such clusters lacking large radio halos are typically found to be more relaxed and less dynamically disturbed (Brunetti et al. 2009), suggesting future modeling improvements (e.g. Vazza et al. 2021).

4.2.3. Sunyaev-Zeldovich and X-ray scaling relations

We proceed to two key observables of the hot ICM. Figure 10 shows the classical Sunyaev-Zeldovich and X-ray scaling relations as a function of halo mass (see also Lim et al. 2021; Truong et al. 2021; Pop et al. 2022, for previous TNG analyses).

In the top panel we show the relation between the thermal SZ signal and halo mass. We compute Y_{SZ} at $z = 0$ in units of pMpc^2 , and so do not include the $E(z)^{-2/3}$ redshift evolution correction, nor the dependence on angular diameter distance d_A^2 . As before, red and blue symbols show halos from TNG300 and TNG-Cluster, respectively. The simulated clusters follow a tight $Y_{500} - M_{500c}$ relation. Its slope is close to the self-similar expectation (dashed line; Kaiser 1986), being only slightly shallower.

We compare the $Y_{\text{SZ},500}$ scaling relation to observations from Planck Collaboration et al. (stars; 2014), where M_{500c} values are derived from an empirical mass-proxy relation using X-ray observations of local clusters from XMM-Newton, under the assumption of hydrostatic equilibrium with calibrated bias. An independent re-analysis of the Planck maps, combined with a SDSS DR7-based group catalog results in a largely consistent relation (dashed line; Hill et al. 2018, their ‘compensated break’ model). However, several issues complicate the comparison with

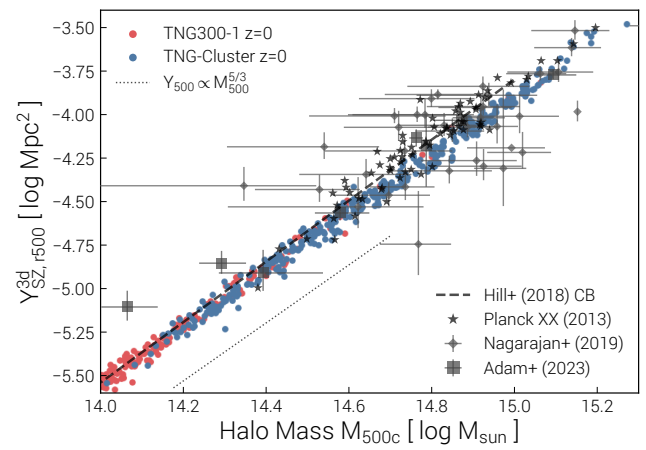


Fig. 10. Sunyaev-Zeldovich (top) and X-ray (bottom) scaling relations versus halo mass (M_{500c}) in TNG-Cluster, and comparison to selected data. **Top:** The $Y_{\text{SZ},500} - M_{500c}$ relation of the simulated clusters is relatively tight and has a slope consistent with the $5/3$ self-similar expectation. We compare to large survey SZ data from Planck (Planck Collaboration et al. 2014; Hill et al. 2018), weak-lensing based cluster mass estimates (Nagarajan et al. 2019), and early NIKA2 observations (Adam et al. 2023). **Bottom:** The integrated $0.5 - 2 \text{ keV}$ cluster luminosity within R_{500c} rises as a function of mass, and with significant scatter. We compare to available X-ray samples at low redshift (Pratt et al. 2009; Vikhlinin et al. 2009; Mantz et al. 2016; Bulbul et al. 2019; Lovisari et al. 2020). The SZ and X-ray scaling relations are both in broad qualitative agreement with data.

simulations. In both cases, the inferred values of M_{500c} can differ from true intrinsic values. Weak lensing allows independent calibration of cluster mass systematics, and results in consistent scaling relations (gray diamonds with errorbars; Nagarajan et al. 2019). Further, the R_{500c} scale for the majority of cluster samples is not well resolved by the large Planck beam, such that the extraction of Y_{500} is complex. Alternatively, comparisons can be made to the Planck data integrating out to a distance of $5R_{500c}$ (e.g. Henden et al. 2018), but at such scales the total tSZ effect begins to probe larger scales, 2-halo gas clustering, and projected contributions more than the cluster gas content itself (Hadzhiyska et al. 2023). In all cases, the resulting two-dimensional projected value must then be converted to Y_{500}^{3d} , which requires additional physical assumptions.

As a result, we present the comparison of the $Y_{500} - M_{500c}$ scaling relation at face value only, and defer consideration of the complex systematics and observational mock details of relevance. In this context, TNG-Cluster is consistent with available

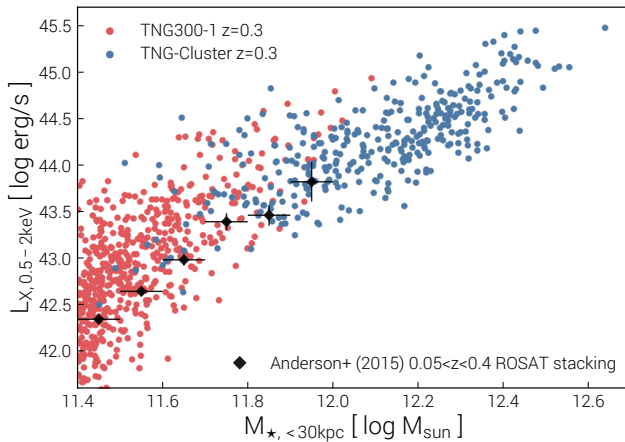


Fig. 11. X-ray scaling relation vs galaxy stellar mass. We show TNG300 (red) and TNG-Cluster (blue) both at $z = 0.3$, which is the average redshift of the observational sample of [Anderson et al. \(2015\)](#), based on ROSAT stacking around locally brightest galaxies from SDSS.

observational constraints. Such a coarse-grained agreement in the integral SZ signal is a common success of most recent cluster simulation projects ([Hahn et al. 2017](#); [Barnes et al. 2017a](#); [Henden et al. 2018](#); [Cui et al. 2018](#); [Pop et al. 2022](#)). Due to its weaker dependence on gas density, it is clearly a less sensitive probe of baryonic and feedback physics than X-ray emission.

Figure 10 (bottom panel) shows the scaling relation between X-ray luminosity and halo mass at $z = 0$. We measure the soft-band (0.5 – 2 keV) integrated luminosity within R_{500c} , as before in 3D (see Section 2.4). Total halo X-ray luminosity increases strongly with mass, rising from $L_{X,r500c} \sim 10^{43.5} \text{ erg s}^{-1}$ for $M_{500c} \approx 10^{14} M_\odot$ to $L_{X,r500c} \sim 10^{45.0} \text{ erg s}^{-1}$ at $M_{500c} \approx 10^{15} M_\odot$. We compare to samples of X-ray observed clusters at low redshift: the 31 X-ray luminosity limited clusters at $z < 0.2$ from the Representative XMM-Newton Cluster Structure Survey (RECESS; [Pratt et al. 2009](#)), the 36 X-ray flux selected clusters, both the low and high redshift samples, observed with Chandra ([Vikhlinin et al. 2009](#)), the diverse sample of 224 clusters, an X-ray flux limited sample, with Chandra and ROSAT data ([Mantz et al. 2016](#)),⁵ the 59 SPT-SZ selected clusters at $0.2 < z < 1.5$ with XMM-Newton followup ([Bulbul et al. 2019](#)), and the 120 Planck-ESZ selected clusters at $z < 0.55$ also with XMM-Newton data ([Lovisari et al. 2020](#)). We always show and compare against ‘core-included’ X-ray luminosities, without excising the core regions (commonly $< 0.15 R_{500c}$), which gives rise to larger scatter than core-excised values ([Pratt et al. 2009](#); [Mantz et al. 2018](#)).

Overall, the $L_{X,500c} - M_{500c}$ scaling relation of TNG-Cluster is broadly consistent with these data sets. Scatter at fixed halo mass is significant at ~ 1 dex, both in observations and in the simulations. The physical origin of this scatter must be understood for cosmological applications of mass-observable relations. While it may be driven primarily by mergers and clusters in different states of relaxedness ([Randall et al. 2002](#)), it may instead be dominated by halo concentration ([Yang et al. 2009](#)) or differences in the central thermodynamical properties ([O’Hara et al. 2006](#)).

Figure 11 shows one further view of the scaling relation between X-ray luminosity and mass: L_X versus galaxy stellar mass.

⁵ Note that the [Mantz et al. \(2016\)](#) sample, with luminosities reported in the wider 0.1 – 2.4 keV band, is converted using the mean ratio of $L_{X,500}^{0.1-2.4\text{keV}} / L_{X,500}^{0.5-2.0\text{keV}} = 1.66$ across the TNG-Cluster sample at $z = 0$.

We compare to observational results which stack ROSAT data on the locations of $\sim 250,000$ locally brightest galaxies from SDSS ([Anderson et al. 2015](#)). The average redshift of this sample is $z \sim 0.3$, where we also show the simulation results. Unfortunately the volume probed by the SDSS main galaxy sample is too small to extend to the most massive galaxies, so this data only overlaps with the low-mass end of TNG-Cluster. Nonetheless, the comparison suggests that halo-scale X-ray emission as function of galaxy mass is in reasonable agreement with data, if perhaps somewhat high. Future stacking experiments with eROSITA beyond the currently available eFEDS field ([Comparat et al. 2022](#); [Chadayammuri et al. 2022](#)) will significantly expand such results.

4.2.4. Radial profiles of ICM metallicity

Existing X-ray observations of clusters enable spatially resolved inferences of key physical properties of the hot ICM. Figure 12 shows radial profiles of three key properties: metallicity (top), temperature (lower left), and entropy (lower right). These are intrinsic, mass-weighted quantities from the simulations, and do not mock the details of any observational measurements. Thin lines show all 352 individual halos from TNG-Cluster at $z = 0$, while the five thick lines show median stacked profiles in 0.2 dex bins of halo mass. The radial and mass trends are diverse.

Metallicity profiles are relatively flat and show only a small (inverse) dependence on halo mass. Our simulated clusters reach $Z \sim 0.5 Z_\odot$ in their centers, decreasing slowly to $\sim 0.3 Z_\odot$ by $0.1 R_{200c}$, and to $\sim 0.1 Z_\odot$ by R_{200c} . However, there is significant halo to halo diversity, and individual clusters can have overall metallicity profiles a factor of two above or below the average (see also [Vogelsberger et al. 2018](#), for previous analysis of cluster metallicities in TNG300).

We compare to a number of observational constraints on the radial gas-phase metallicity profiles of clusters: the sample of 207 groups and clusters at $z < 0.1$ with XMM-Newton coverage ([Lovisari & Reiprich 2019](#)),⁶ the mixture of 50 cool-core and non-cool-core clusters at $0.1 < z < 0.3$ also with X-ray data from XMM-Newton ([Leccardi & Molendi 2008](#)), the outskirts constraint from [Molendi et al. \(2016a\)](#) which is an extrapolated, rough upper limit, and the X-COP sample ([Eckert et al. 2017](#)) of 13 $z < 0.1$ high-mass clusters with $M_{500} > 3 \times 10^{14} M_\odot$ and large field of view coverage ([Ghizzardi et al. 2021](#)).

Observations broadly infer that cluster metallicity profiles can be high in cluster cores, reaching values $\sim 0.5 - 0.8 Z_\odot$ (especially for cool-core systems), but decreasing to $\sim 0.2 - 0.3 Z_\odot$ for $R \gtrsim 0.2 R_{500c}$, beyond which radial metallicity profiles are relatively flat. This may reflect feedback-driven metal redistribution from the central BCG itself ([Gitti et al. 2012](#)), that most metals are already produced in the cores of cluster progenitors at high redshift ([Pearce et al. 2021](#)), or the collective effect of environmental pre-enrichment in an overdense region at earlier times ([Vogelsberger et al. 2018](#); [Biffi et al. 2018](#)).

Overall, TNG-Cluster is in reasonable agreement with observed ICM metallicity profiles, particularly in the radial trend. The simulated profiles are plausibly too low, by $\sim 0.1 Z_\odot$, regardless of distance. However, without a detailed forward modeling effort, we leave more quantitative comparisons for future work. Unfortunately, the systematics involved in observational estimates of ICM metallicity from X-ray spectra are significant,

⁶ We re-scale all normalizations from each assumed solar metallicity value to the TNG value of $Z_\odot = 0.0127$. We also re-scale from R_{500c} to R_{200c} values where necessary, using the average ratio of $R_{500c}/R_{200c} = 0.65$ for the TNG-Cluster sample at $z = 0$.

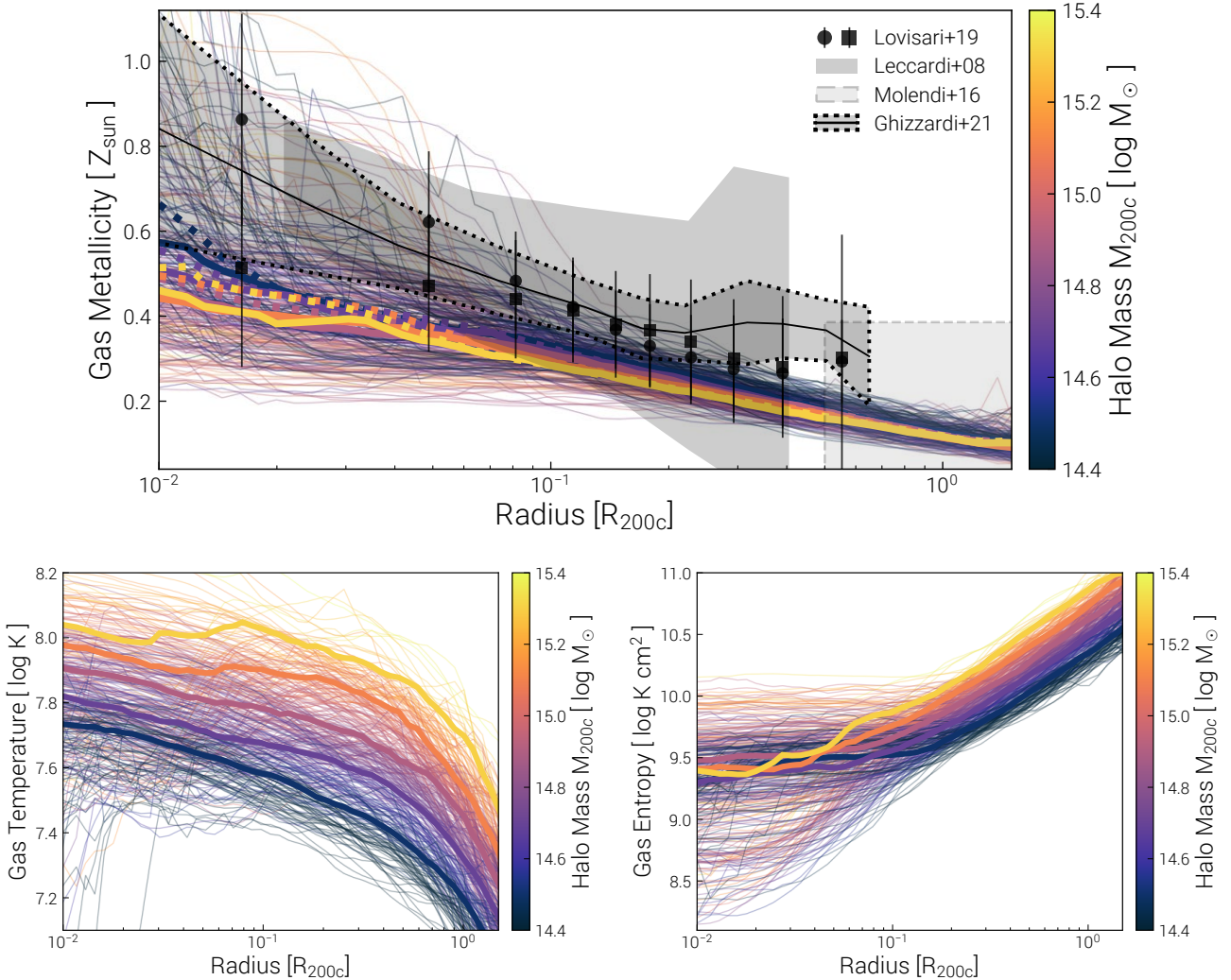


Fig. 12. Radial profiles of ICM metallicity (top), temperature (lower left), and entropy (lower right) of the complete TNG-Cluster sample at $z = 0$. In all three panels thin lines show the 352 individual clusters, colored by halo mass, while the five thick lines show median provides in 0.2 dex halo mass bins. For metallicity, we also include mean stacked profiles as thick dotted lines. Profiles include all gas and are mass-weighted. We compare the metallicity profiles to observational inferences for low-redshift clusters (Leccardi & Molendi 2008; Molendi et al. 2016a; Lovisari & Reiprich 2019; Ghizzardi et al. 2021, see text).

making comparisons beyond the factor of ~ 2 level difficult (Molendi et al. 2016a).⁷ Future X-ray instruments with high spectral resolution will improve our observational census of cluster metals significantly (Mernier et al. 2023).

4.2.5. Radial profiles of ICM temperature and entropy

Figure 12 also shows temperature (lower left) and entropy (lower right) profiles of TNG-Cluster at $z = 0$. Most temperature profiles rise in overall normalization with the halo virial temperature, and monotonically decrease with increasing radius. However, a subset of clusters show central temperature depressions indicative of strong cool cores (see the companion paper by Lehle et al. 2023). There is similar diversity in cluster entropy profiles. While many halos have high central entropy (K_0), indicative of non-cool-core

(NCC) clusters, others have K_0 values an order of magnitude lower, highlighting cool-core (CC) clusters. Although K_0 , as well as central cooling time and density, all increase with halo mass, this CC vs NCC heterogeneity of the cluster population occurs even at fixed halo mass (see Lehle et al. 2023).

The kinematics of the ICM, and comparisons to observations, are presented in the TNG-Cluster companion papers by Truong et al. (2023) and Ayromlou et al. (2023b).

5. Properties of the Galaxies

We now turn our attention to the properties of galaxies residing within TNG-Cluster halos. First, in terms of their SMBHs, cool gas content and star formation activity, their stellar masses, and finally to the satellite galaxy populations they host.

5.1. Supermassive black holes

Figure 13 shows the scaling relation between central SMBH mass and total halo mass (left; Ferrarese 2002) as well as central

⁷ Although we show TNG-Cluster profiles at $z = 0$, the typical redshift of observed clusters is higher. We note that the simulated profiles shift down by $\sim 0.05 Z_{\odot}$ at $z = 0.2$ (not shown). X-ray emission weighting, as opposed to mass weighting, has a negligible impact. Profiles in 2D projection instead of 3D are also lower by $\sim 0.05 Z_{\odot}$.

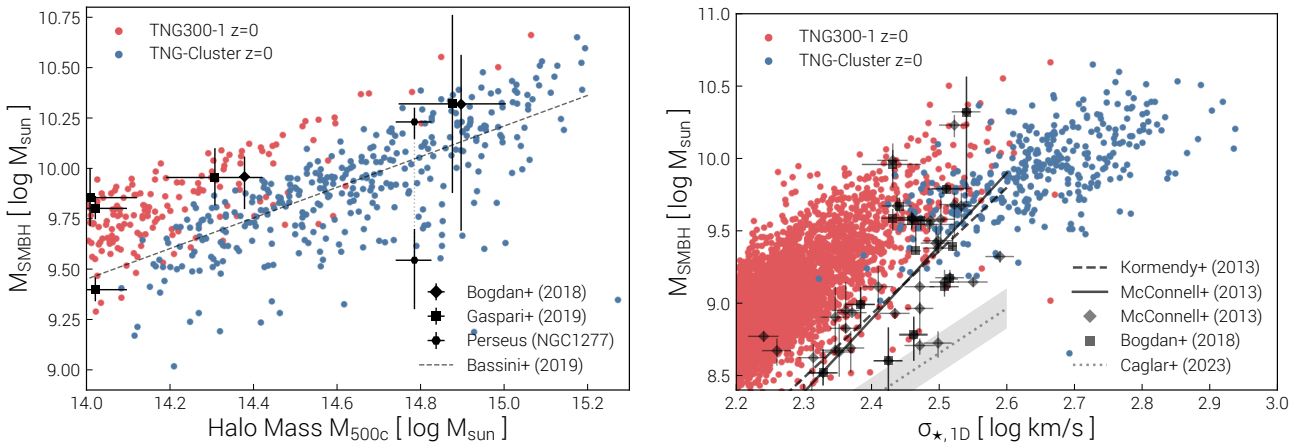


Fig. 13. SMBH mass scaling relations, as a function of total halo mass (left) and stellar velocity dispersion (right). We adopt the most massive SMBH of each BCG, if several are present, and measure σ_* based on the 1D line-of-sight stellar kinematics within an aperture of 10 pkpc (see text). We compare to observational scaling relations (Kormendy & Ho 2013; McConnell & Ma 2013), as well as measurements for group and cluster BCGs (Bogdán et al. 2018; Gaspari et al. 2019). Note that the scaling relations are largely extrapolations in the TNG-Cluster regime. We also include two inferences for NGC1277 of Perseus (see text), and compare to the simulation results of Bassini et al. (2019). The most massive SMBHs in TNG-Cluster reach $4 - 5 \times 10^{10} M_\odot$, although SMBH growth slows down in the cluster regime, somewhat flattening the scaling relations.

stellar velocity dispersion (right; Magorrian et al. 1998). We include only the central i.e. BCGs of each cluster, take the most massive SMBH if there are several present, and measure the one-dimensional, mass-weighted $\sigma_{*,1D}$ along a random line-of-sight direction, within an aperture of 10 kpc, to capture the central dynamics of BCGs.

We compare to a number of observationally inferred relations (Kormendy & Ho 2013; McConnell & Ma 2013; Caglar et al. 2023), as well as to observational samples of group and cluster BCGs (Bogdán et al. 2018; Gaspari et al. 2019). In addition, we indicate the SMBH of the Perseus cluster (NGC1277) with $M_{\text{SMBH}} = 2 - 20 \times 10^9 M_\odot$ (encompassing 1σ estimates from van den Bosch et al. 2012; Emsellem 2013) and $M_{500c} = 6.1 \pm 0.6 \times 10^{14} M_\odot$ (Giacintucci et al. 2019). Finally, we include the scaling relation found in the Dianoga cluster zoom simulations for comparison (Bassini et al. 2019).

Comparison of the trends of SMBH masses with halo and galaxy properties in TNG-Cluster versus data is not straightforward. The values of M_{SMBH} as a function of halo mass are broadly consistent with the small samples available, although any statistical comparison is impossible. With respect to the $M_{\text{SMBH}} - \sigma_*$ relation, we emphasize that observational scaling relations are almost entirely extrapolations in this regime, as direct measurements of SMBH scaling relations for massive BCGs with $M_{500c} \gtrsim 10^{14} M_\odot$, or $\sigma_* \gtrsim 400 \text{ km s}^{-1}$, are exceedingly rare. As a result, small differences in slope lead to large differences in anticipated SMBH mass for such massive BCGs. In addition, the values of σ_* extracted from the simulations depend on, and increase with, aperture (Sohn et al. 2022). If we instead measure σ_* within the stellar half mass radius (i.e. the effective radius), this would shift values slightly to the right. However, we emphasize that our measurement of stellar velocity dispersion is not forward modeled and differs in numerous respects from methods used to infer σ_* from data, including the use of effective velocity dispersion (Sijacki et al. 2015), preventing any quantitative comparisons for the time being.

The $M_{\text{SMBH}} - \sigma_*$ relation, as well as the $M_{\text{SMBH}} - M_*$ relation (not shown) both become shallower and level off in the cluster regime. This is partly due to lower SMBH masses in TNG-Cluster versus TNG300, which we discuss below in the context of stellar

masses. This trend may also reflect a shift in the physics of SMBH growth: it coincides with the mass scale where halos retain their full baryon fractions (Ayromlou et al. 2023a), and thus the energetics of SMBH feedback are no longer sufficient to significantly impact the baryon distribution and thermodynamical properties of the ICM (Voit et al. 2023). Indeed, the slope of the underlying $M_{\text{SMBH}} - M_{\text{halo}}$ relation (Marasco et al. 2021) evolves from super-linear to sub-linear at high masses, while the scatter decreases, reflecting a natural outcome of the hierarchical assembly process (Truong et al. 2021).

5.2. Cool Gas and Star Formation Activity

Figure 14 shows the distribution of galactic star formation rates (SFRs, left panel) as a function of halo mass at $z = 0$. We include only the central galaxy (BCG) of each cluster, and show instantaneous SFRs. Values of absolute zero in the simulation result from our finite resolution (Donnari et al. 2019), and for TNG-Cluster these correspond physically to upper limits of $< 10^{-3} M_\odot \text{yr}^{-1}$. These systems are placed at this value, with $\pm 0.5 \text{ dex}$ scatter added for visual clarity.

The vast majority of central cluster galaxies in TNG-Cluster are quenched. The gray shaded triangular region (left panel) indicates the canonical $z = 0$ quiescent threshold of $\text{sSFR} < 10^{-11} \text{ yr}^{-1}$, and only $\sim 8\%$ of TNG-Cluster BCGs are star-forming according to this definition. Adding in the galaxies with residual (non-zero) SFR, the TNG-Cluster fraction increases to $\sim 13\%$. The vast majority of star-forming BCGs reside in cool-core clusters, as marked by small black crosses in the panel (see the companion paper by Lehle et al. 2023). There is no strong halo mass trend in star formation activity (as seen in Orellana-González et al. 2022), although observations infer an increasing star-forming fraction with cluster richness (Liu et al. 2012). The overall star-forming fraction from TNG-Cluster is similar to fraction of star-forming cluster BCGs in McDonald et al. (2016) based on a sample of 90 SPT selected clusters, where a strong trend with redshift towards mostly star-forming BCGs at $z \gtrsim 1$ is evident as well (see also Bonaventura et al. 2017).

The origin of the fuel for this ‘residual’ star-formation is unclear. The relatively small fraction of star-forming BCGs suggests

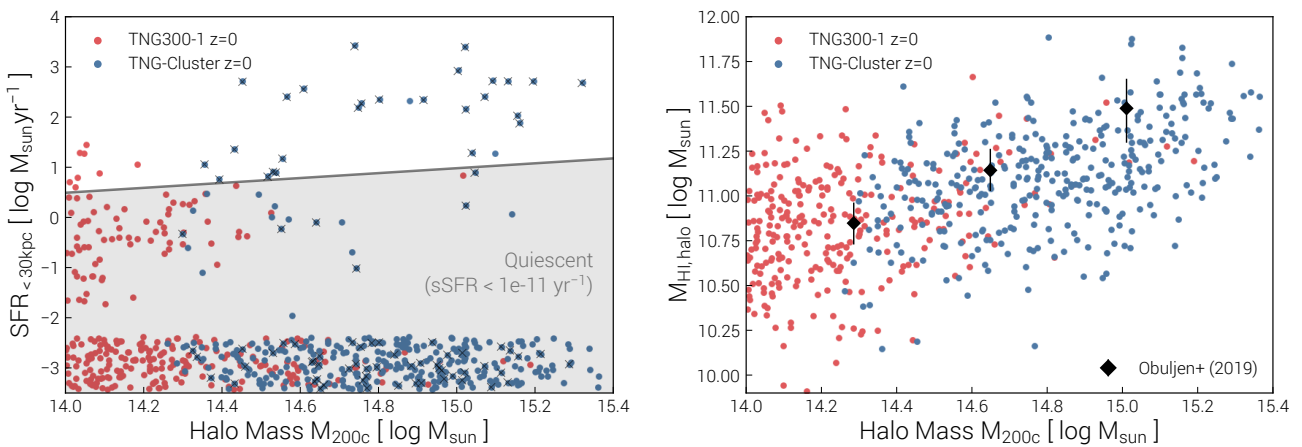


Fig. 14. Star formation activity and cold gas contents. **Left:** Galaxy star formation rate as a function of halo mass, at $z = 0$. A quiescent threshold of $\text{sSFR} < 10^{-11} \text{ yr}^{-1}$ is indicated as the gray triangular region, adopting the stellar mass to halo mass relation of TNG-Cluster. Black crosses mark those clusters identified as strong cool-cores with the fiducial criterion of (Lehle et al. 2023). The vast majority of central galaxies in clusters are quenched, and only a small number have non-negligible levels of residual star formation. **Right:** Total cold (HI) mass in the halo as a function of mass, compared to observations stacking ALFALFA data on SDSS groups and clusters (Obuljen et al. 2019).

a short duty-cycle of high SFR activity, which could be driven either by episodic – possibly ‘hidden’ – cooling flows from the hot ICM (Molendi et al. 2016b; Fabian et al. 2023) that are subsequently terminated by AGN feedback (Voit et al. 2015; Calzadilla et al. 2022), or by cosmologically rare gas-rich mergers (Webb et al. 2015). In either case, this suggests that in-situ star formation, and not solely ex-situ dry mergers, contribute to cluster BCG formation: whereas this is expected particularly at high redshift and in the protocluster regime (Montenegro-Taborda et al. 2023), our findings show that, in a fraction of BCGs, this is the case also at the current epoch.

Figure 14 also shows the total mass of neutral HI in the halo, as a function of halo mass at $z = 0$ (right panel). Although the fraction of neutral HI relative to the total halo gas mass is small, $M_{\text{HI}}/M_{\text{gas}} \sim 10^{-4} - 5 \times 10^{-3}$, in absolute terms there is an enormous amount of such cool $\sim 10^4$ K gas in clusters. We therefore compare to observational results that stack large-beam ALFALFA survey data at the locations of $z \sim 0$ SDSS groups and clusters (Obuljen et al. 2019). We note that this comparison is intended at face-value only, as we measure 3D total halo masses for the simulations, versus 2D projected values over large beam sizes from ALFALFA. For any non-zero line-of-sight contribution, the former is a lower limit on the latter. Regardless, the mass of HI gas in TNG-Cluster halos is in the ballpark of low-redshift observational inferences (see also Zhang et al. 2020b).

Observations suggest that significant amounts of molecular gas are common although not ubiquitous in star-forming BCGs (Castignani et al. 2020; Dunne et al. 2021). Unsurprisingly, large amounts of cool gas correlate with central cooling flows as well as starbursts (Edge 2001). Cool gas is also prevalent throughout clusters, as mapped in detail for local examples including Virgo with H α narrow-band imaging (VESTIGE; Boselli et al. 2018) and Fornax with MeerKAT (Serra et al. 2016). High-mass halos hosting rich satellite populations in the TNG simulations similarly have large amounts of cool gas with complex morphologies and frequent ram-pressure stripping origins (Yun et al. 2019; Nelson et al. 2020; Rohr et al. 2023b; Zinger et al. 2023). The contributions of satellites to the cluster ICM in TNG-Cluster is the subject of a companion paper (Rohr et al. 2023a).

5.3. Stellar Content

We conclude this overview of TNG-Cluster by quantifying the stellar mass content of our simulated halos and their satellites (see Pillepich et al. 2018a, for previous TNG analyses) Figure 15 shows the stellar masses of TNG-Cluster central galaxies (left) as well as total halo stellar masses (right). We define the former using a 3D radial aperture of 30 pkpc, and the latter as all stars within R_{500c} (excluding satellites).

We compare galaxy stellar masses to a number of observational constraints (left panel), noting however that at such high masses BCG stellar mass measurements are becoming less statistical as well as more sensitive to measurement technique and observational details (D’Souza et al. 2015). We compare to semi-empirical inferences i.e. older abundance matching type results (Behroozi et al. 2013; Moster et al. 2013) as well as their newer counterparts (Behroozi et al. 2019; Moster et al. 2020). The updated models infer significantly higher stellar masses at fixed halo mass. However, the semi-empirical models are all based on stellar mass functions derived from photometry which is non-ideal for massive galaxies and underestimates their total stellar masses considerably. The 30 pkpc aperture is chosen to roughly replicate these measurements (Schaye et al. 2015; Pillepich et al. 2018a). We also compare to direct optical/infrared measurements of BCGs in 21 clusters at $z \lesssim 0.1$, integrating stellar light out to $\sim 100 - 300$ kpc, with total halo masses derived from X-ray data (Kravtsov et al. 2018). In addition, we contrast against the X-ray selected HSC-XXL sample with weak lensing based halo mass estimates (Akino et al. 2022), as well as the low and intermediate redshift BCG sample of DeMaio et al. (2020), including some CLASH targets (see also Lin et al. 2012).

Broadly speaking, observational inferences of BCG stellar masses are broadly consistent with the low-mass end of the cluster distribution. This is the case in particular where our sample is dominated by TNG300. The situation is less clear for the most massive clusters with $M_{500c} \gtrsim 10^{14.5} M_{\odot}$ where observations become rare. Nonetheless, the TNG-Cluster sample has BCG stellar masses that are plausibly too large, by $\sim 0.1 - 0.2$ dex in the mean. If we compare data to the simulated clusters at $z = 0.3$ instead of $z = 0$ (not shown), the typical median redshift of observed cluster samples, the situation is improved but not

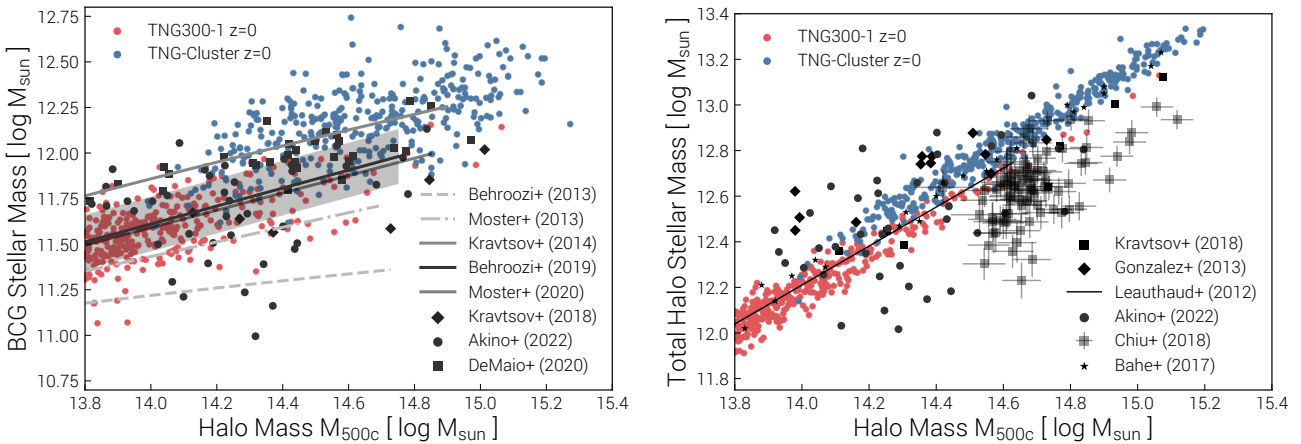


Fig. 15. The stellar content of TNG-Cluster halos: stellar mass of the central galaxy i.e. BCG (left), and total stellar mass of the halo i.e. the central galaxy together with the extended ICL as well as satellites (right). For central galaxy stellar mass we sum stars within $r < 30$ pkpc, and compare to abundance matching results (Behroozi et al. 2013; Moster et al. 2013; Behroozi et al. 2019; Moster et al. 2020) and observational inferences using similar definitions (Kravtsov et al. 2018; DeMaio et al. 2020; Akino et al. 2022). For total halo stellar mass we sum stars within $r < r_{500c}$, and also compare to data using similar definitions (Leauthaud et al. 2012; Gonzalez et al. 2013; Kravtsov et al. 2018; Chiu et al. 2018; Akino et al. 2022) as well as the Hydrangea simulations (Bahé et al. 2017).

entirely so. This could suggest that the SMBH feedback model in TNG, which has never been evaluated in such massive halos, does not suppress star formation in these BCGs. More likely, since the stellar mass content of such massive galaxies are $> 90\%$ ex-situ in origin (Rodriguez-Gomez et al. 2015; Pillepich et al. 2018a), it may indicate too much stellar mass growth during earlier i.e. proto-cluster phases. Comparison of resolved stellar mass profiles will shed light on this (Ardila et al. 2021), although targeted imaging campaigns are needed to build a sample of the highest mass clusters.

We also compare total halo stellar masses to a number of observational constraints (right panel). In particular, the same samples as previously (Gonzalez et al. 2013; Kravtsov et al. 2018; Akino et al. 2022), as well as a halo occupation distribution analysis of the COSMOS data at slightly higher redshift $z \sim 0.4$ (Leauthaud et al. 2012). The observational points again scatter about the combined simulation results, albeit with significantly larger scatter. We also compare to the SZ-selected sample of 91 clusters with $0.2 < z < 1.25$ with photometric estimates on combined BCG and satellite stellar masses (Chiu et al. 2018). This data falls ~ 0.2 dex below the simulations, but does not detect nor include the ICL component, and has a notably higher mean redshift. Constraints on the total halo stellar mass at $M_{500c} \gtrsim 10^{15} M_{\odot}$ are unfortunately exceedingly sparse, and it is hard to draw any statistical comparisons.

Both panels of Figure 15 also hint towards a steepening and/or normalization offset of the stellar mass to halo mass relations between TNG300 and TNG-Cluster. Given that they employ the same physical galaxy formation model, at the same resolution, this is unexpected. The recent MTNG simulation found a similar effect in their large hydrodynamical box (MTNG740; Pakmor et al. 2023b), namely that stellar masses were more similar to TNG100 than TNG300, at odds with our analysis of stellar mass convergence with resolution in the TNG model (Pillepich et al. 2018a). Instead, galaxy stellar masses are consistent with a higher, TNG100-like resolution. Pakmor et al. (2023b) attribute this to the exclusion of magnetic fields in MTNG, and the interaction of magnetic fields with the kinetic SMBH feedback mode of the TNG model. However, since we include magnetic fields in TNG-Cluster, we can rule out this possibility.

In TNG-Cluster we find that the ‘steeper’ star-formation timescale change, originally developed and applied in TNG50 (see Section 2.2 of Nelson et al. 2019b), is the clearest cause. While we verified that this change made no difference to galaxy properties for TNG50, this was only possible to study for $M_{200c} < 10^{14} M_{\odot}$ halos. In massive clusters, it appears that the acceleration of star-formation for the densest gas leads to a more rapid conversion of nuclear gas into stars. As a result, central gas densities are slightly lower, which causes lower accretion rates onto SMBHs, and lower overall kinetic-mode energy output. In turn, SMBH masses are reduced, and stellar masses increased, with respect to a TNG300 resolution simulation. In net effect, this means that many of the physical properties of TNG-Cluster galaxies are in fact more similar to a TNG100 resolution simulation, which is largely advantageous as this is the resolution that the model was calibrated at (Pillepich et al. 2018b). The magnitude of this effect is $\sim 30 - 40\%$ in mass, i.e. the same as the change in stellar masses from TNG100 to TNG300 resolution, and we do not expect it to significantly affect any conclusions or analyses of TNG-Cluster.

5.4. Satellites

Returning to the results of TNG-Cluster, we briefly consider the satellite galaxy populations. Figure 16 shows the galaxy surface density i.e. radial number density profiles of galaxies surrounding TNG-Cluster halos at $z = 0$. We stack mean profiles in five halo mass bins, as indicated in the legend (see also Riggs et al. 2022, for related analysis with TNG300). Solid lines include galaxies satisfying $M_r < -20.5$, in order to match observational selections, using the fiducial resolved dust modeling of Nelson et al. (2018b) to derive stellar light.⁸ We project along a line-of-sight depth of ± 5 Mpc and average over three independent projection directions for each curve. The three sets of fainter, dashed lines show three stellar mass cuts. The lowest set of dashed curves corresponds to $M_{\star} > 10^{11.5} M_{\odot}$, while the middle set includes

⁸ For comparison, the dotted lines show stellar magnitudes neglecting dust. Different color modeling assumptions have only a minor impact. Neglecting dust increases galaxy counts by $\sim 50\%$. Different projection depths also have marginal impact, slightly increasing counts at $\gtrsim 1$ Mpc.

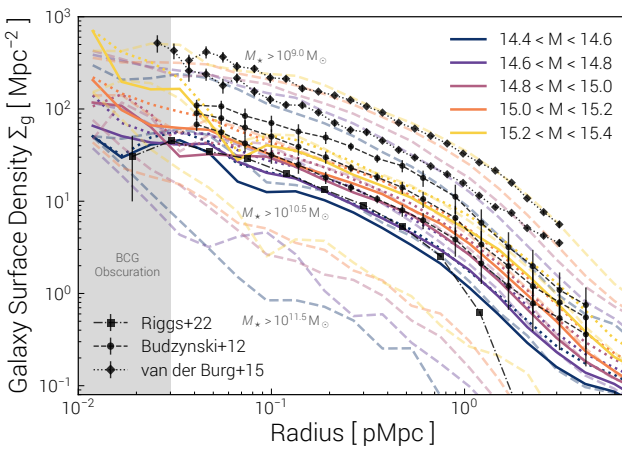


Fig. 16. The radial distribution of nearby (satellite) galaxies, from the centers of TNG-Cluster halos at $z = 0$. We show the surface number density, i.e. number of galaxies per Mpc^2 , as a function of distance. We stack around clusters in five halo mass bins, as indicated in the legend for M_{200c} in $\log M_\odot$. We include galaxies with $M_r < -20.5$ mag (thick solid lines including dust modeling, dotted lines without; see text) in order to match observational constraints from SDSS (Budzynski et al. 2012, black circles and dashed lines;). We also compare to data from GAMA (black squares and dot-dash line; Riggs et al. 2022). In addition we include stellar mass based constraints with three additional sets of dashed colored lines: $M_\star > \{10^9, 10^{10.5}, 10^{11.5}\} M_\odot$. The first i.e. highest set of colored curves are comparable to observational constraints from van der Burg et al. (2015, see text).

galaxies with $M_\star > 10^{10.5} M_\odot$ – the median stellar mass at this absolute magnitude threshold. Finally, the highest set of dashed curves shows lower mass galaxies with $M_\star > 10^9 M_\odot$, a regime inaccessible in large sky surveys (Lin et al. 2004) but available with targeted cluster surveys (van der Burg et al. 2015).

The three have notably different radial behavior, with $\Sigma_{\text{gal}}(r)$ declining most slowly (rapidly) for the lower (higher) stellar mass samples. Galaxies with a Milky-Way like stellar mass of $M_\star > 10^{10.5} M_\odot$ or higher are found with a density of $\sim 100 \text{ Mpc}^{-2}$ in the centers of clusters, where obscuration by the central galaxy at $\lesssim 30 \text{ kpc}$ makes their identification in data challenging. Their density drops by a factor of one hundred, to $\sim 1 \text{ Mpc}^{-2}$ at a halocentric distance of 1 Mpc. In all cases, a host halo mass trend is present: more massive clusters are surrounded by more satellite and neighboring galaxies. Σ_{gal} increases by roughly a factor of two, at any distance, for a factor of ten increase in host M_{200c} . This reflects the underlying dependence of richness on cluster mass – we refer to the companion paper (Rohr et al. 2023a) for an analysis of satellite counts i.e. cluster richness and the corresponding comparison with observations.

With respect to data, broad agreement with the radial number density and color profiles of satellite galaxies around massive hosts was a noted success of the original Illustris simulation (Vogelsberger et al. 2014; Sales et al. 2015), in contrast to semi-analytical models at the time (Wang et al. 2014). Here, we compare to observational measurements based on stacking of clusters from SDSS at $0.15 < z < 0.4$, with halo mass estimates from optical richness (Budzynski et al. 2012). From that work we show three sets of black markers, corresponding to three M_{500} halo mass bins in $\log M_\odot$: $14.0 - 14.4$, $14.4 - 14.7$, and $14.7 - 15.0$ (from lowest to highest). In all cases neighboring galaxies are included if they satisfy an absolute magnitude threshold of $M_r < -20.5$, and should therefore be compared to the thick colored lines from TNG-Cluster. While the radial

shape of $\Sigma_{\text{gal}}(r)$ is remarkably similar with the data, the simulations appear offset to lower amplitudes. However, the trends with threshold stellar mass (or r -band magnitude) suggest that such differences can reflect biases as small as ~ 0.1 dex in M_\star or M_r .

We therefore also compare to radial satellite profiles inferred from the GAMA survey, using a substantially different, friends-of-friends halo member identification methodology ($r < 19.8$; Riggs et al. 2022, including a comparison with TNG300). In particular, we show the highest halo mass bin available, for $13.7 < \log M_{200m}/M_\odot < 14.8$ at $z < 0.27$ (black squares and line). We do not try to reproduce the methodology in detail, and offer it as a face value comparison. The overall shape of $\Sigma_{\text{gal}}(r)$ is similar to TNG-Cluster, while the normalization suggests a best-match with our $M_{200c} \sim 10^{14.7} M_\odot$ bin.⁹

We also compare to the radial galaxy number density measured around a sample of 60 massive clusters at $z < 0.26$, based on deep $ugri$ -band photometry (van der Burg et al. 2015, diamonds and dotted lines). Halo masses are based on the Evrard et al. (2008) scaling relation from member velocity dispersion σ_v , which is itself inferred from spectroscopically confirmed cluster members. We show two results: for galaxies with $10^9 < M_\star/M_\odot < 10^{10}$ (upper curve) and for $M_\star > 10^{10} M_\odot$ (lower curve).¹⁰ With a mean halo mass of $M_{200} \simeq 10^{14.8} M_\odot$, the sum of the two lines is best compared to the middle colored line in the $M_\star > 10^9 M_\odot$ group from TNG-Cluster. As above, the radial shape of $\Sigma_{\text{gal}}(r)$ is in excellent agreement, while the observations suggest a somewhat higher normalization. In general, galaxy radial profiles are understood to be quite similar to lensing i.e. total matter profiles in cluster outskirts, though not necessarily in their cores, suggesting inside-out i.e. hierarchical assembly (Wang et al. 2018a; Shin et al. 2021).

These radial profiles of galaxy counts reflect the rich satellite galaxy populations of clusters. Simultaneously, the physical properties of those galaxies capture the process of galaxy evolution in such dense environments. By self-consistently modeling the stellar and gaseous bodies of the galaxy populations embedded within the ICM and dark matter halos of galaxy clusters, TNG-Cluster sheds light on the intertwined physical processes that shape some of the most massive structures in the Universe.

6. Summary and Conclusions

In this paper we introduce the new TNG-Cluster project, a suite of cosmological magnetohydrodynamical simulations of high-mass galaxy clusters. Adopting the IllustrisTNG galaxy formation model, we simulate 352 clusters spanning a halo mass range of $\log(M_{200c}/M_\odot) \gtrsim 14.5 - 15.4$ at $z = 0$. We present the simulations, and first results on the sample and key physical properties, spanning halo assembly and dark matter, to cluster galaxies and their stars, the intracluster medium (ICM), and the supermassive black hole (SMBH) population. Our main results are:

- The statistics of TNG-Cluster (Figure 1) are well matched to compare to the largest current observational surveys of galaxy clusters (Figure 3), as detected in Sunyaev-Zeldovich (SZ) effect surveys including Planck, ACT-SZ DR5, and SPT-ECS; in X-ray emission with ROSAT, eROSITA, XMM-Newton XXL 365; and in the optical with SDSS, HSC x SpARCS,

⁹ The rapid drop in the GAMA profiles at distances $\gtrsim 1 \text{ Mpc}$ are understood to stem from the FoF algorithm (see Riggs et al. 2022).

¹⁰ R_{200} scaled observational values are converted with the mean $R_{200} = 1.7 \text{ Mpc}$ of the sample.

- and more. The $z = 0$ cluster progenitors reveal the assembly of these massive structures at higher redshifts, including protoclusters phases at $z \sim 1$ and $z \sim 2$.
- TNG-Cluster is currently the largest sample of simulated clusters at comparable numerical resolution, with ~ 90 halos at $M_{200c} > 10^{15} M_\odot$ (Table 1). Compared to projects with similar statistics, its (mass) resolution is 10x to 100x better, with $m_{\text{baryon}} = 10^7 M_\odot$ (Figure 4). It also includes the comprehensive, well-validated, and empirically constrained TNG galaxy formation model. By increasing the cluster sample previously available in the TNG300 simulation at unchanged model and resolution, we are able to quantitatively test this model in the high-mass regime, and explore a rich variety of physical phenomena in galaxy clusters (Figure 5).
 - Halo gas fractions rapidly approach the cosmic baryon fraction, as expected for the most massive halos. There is no mass trend for clusters with $M_{500c} \gtrsim 10^{14.5} M_\odot$. This is consistent with X-ray and SZ data (Figure 7).
 - Halo magnetic field strength increases with cluster mass, and towards higher redshift. Volume-weighted mean $|B|$ field strengths in the inner halo reach $\sim \mu\text{G}$ values, consistent with the few available observational measurements (Figure 8).
 - Radio synchrotron emission ($P_{1.4\text{GHz}}$), modeled in postprocessing, shows a tight relation with halo mass, reaching $10^{25} \text{ W Hz}^{-1}$ for our most massive clusters, consistent with data (Figure 9). Radio relics and the structure of radio emission in TNG-Cluster is studied in detail in a companion paper (Lee et al. 2023).
 - The scaling relations of Sunyaev-Zeldovich y-parameter, and soft-band X-ray luminosity from $0.5 - 2 \text{ keV}$, both measured within R_{500c} , are in reasonable agreement with available data (Figure 10), as is halo X-ray luminosity as a function of galaxy stellar mass (Figure 11). These relations have non-negligible scatter that encodes the physics of halo assembly and baryonic physics.
 - Radial profiles of ICM metallicity are remarkably flat, and broadly consistent with observations. Profiles of temperature and entropy are diverse, reflecting the diversity of the cluster population and the co-existence of cool-core and non-cool-core ICM structure, even at fixed halo mass (Figure 12).
 - Cluster BCGs host SMBHs with masses as high as $4 - 5 \times 10^{10} M_\odot$, and the relation between SMBH mass and M_{500c} is consistent with the small observational samples at such high masses (Figure 13, left panel). The relation between M_{SMBH} and stellar velocity dispersion σ_* , flattens in the cluster regime (Figure 13, right panel), potentially reflecting a shift in the physics of SMBH growth and how AGN feedback interacts with gaseous halos. The impact of SMBH feedback on the resolved structure of the ICM is the subject of a companion paper (Pillepich et al. in prep.).
 - The vast majority of central galaxies in TNG-Cluster are quiescent, with specific star formation rates $\text{sSFR} < 10^{-14} \text{ yr}^{-1}$. However, a small but non-negligible fraction exhibits activity up to $\text{SFR} \gtrsim 100 - 1000 M_\odot \text{ yr}^{-1}$ (Figure 14). The resulting star-forming BCG fractions (or quenched fractions) as a function of galaxy mass are in broad agreement with observations.
 - Star-forming BCGs are preferentially in cool-core (CC), as opposed to non-cool-core (NCC) clusters. TNG-Cluster produces a diversity of strong CC, weak CC, and NCC halos, studied in a companion paper (Lehle et al. 2023).
 - The ICM is multi-phase. In particular, cluster halos contain non-vanishing amounts of cool gas, including neutral HI. The M_{HI} increases with halo mass, and is the ball park of observational data (Figure 14, right panel).
- Kinematics and turbulence in cluster cores are studied in detail in a companion paper (Truong et al. 2023), while velocity structure across the halo and into the outskirts is the focus of Ayromlou et al. (2023b).
- Stellar masses of cluster BCGs occupy a similar parameter space as a function of halo mass as observations, although they are above some semi-empirical models and mean values for available samples by ~ 0.2 dex (Figure 15). This may indicate insufficient star-formation suppression by the SMBH feedback model of TNG, either at late times or in proto-cluster phases at $z \sim 1 - 2$.
- Satellite populations are rich, and their overall abundance and radial distribution increases with halo mass in agreement with data (Figure 16). The satellite galaxy population, and their gaseous contents in particular, is the focus of a companion paper (Rohr et al. 2023a).

By surveying a broad range of physics, physical processes, physical properties, and observable outcomes, we emphasize the breadth of TNG-Cluster and its many potential applications. In fact, the majority of the comparisons to observations presented in this paper are intended at face value only, as we have not replicated in detail observational effects. As a result, we expect that each of the scientific topics explored here will be revisited in more depth in future work.

Practically, TNG-Cluster achieves high resolution due to its nature as a suite of individual zoom simulations. This is in contrast to large uniform volume simulations such as MillenniumTNG and FLAMINGO. By trading resolution for volume they can probe questions that TNG-Cluster cannot, such as large-scale galaxy clustering, and cosmological projection i.e. lightcone effects on observables. In contrast, TNG-Cluster focuses on the details and structure of cluster halos, the ICM, the galaxy populations in and near high-mass halos, including their SMBHs, and the assembly of all these components across cosmic time.

TNG-Cluster is unique in several model aspects, including in its modeling of magnetic fields. An assessment of the level of (dis)agreement with observational data in the cluster mass regime will benefit from more detailed, quantitative comparisons in the future. In addition, other potentially important (plasma) physics processes of interest for the ICM are not yet treated. These include (anisotropic) thermal conduction, radiative transfer, and non-continuum i.e. kinetic effects, as well as relativistic particle populations such as cosmic rays, and relativistic outflows/jets launched by SMBHs. While these complex physical processes have been explored in idealized contexts, their inclusion in full cosmological simulations remains a future goal.

Data Availability

The IllustrisTNG simulations themselves are publicly available and accessible at www.tng-project.org/data, as described in Nelson et al. (2019b), where the TNG-Cluster simulation will also be made public in 2024. Data directly related to this publication is available on request from the corresponding author.

Acknowledgements

DN and MA acknowledge funding from the Deutsche Forschungsgemeinschaft (DFG) through an Emmy Noether Research Group (grant number NE 2441/1-1). This work is co-funded by the European Union (ERC, COSMIC-KEY, 101087822, PI: Pillepich). KL acknowledges funding from the

Hector Fellow Academy through a Research Career Development Award. KL and ER are fellows of the International Max Planck Research School for Astronomy and Cosmic Physics at the University of Heidelberg (IMPRS-HD). NT acknowledges that the material is based upon work supported by NASA under award number 80GSFC21M0002. This work is supported by the Deutsche Forschungsgemeinschaft (DFG, German Research Foundation) under Germany's Excellence Strategy EXC 2181/1 - 390900948 (the Heidelberg STRUCTURES Excellence Cluster).

The TNG-Cluster simulation suite has been executed on several machines: with compute time awarded under the TNG-Cluster project on the HoreKa supercomputer, funded by the Ministry of Science, Research and the Arts Baden-Württemberg and by the Federal Ministry of Education and Research; the bwForCluster Helix supercomputer, supported by the state of Baden-Württemberg through bwHPC and the German Research Foundation (DFG) through grant INST 35/1597-1 FUGG; the Vera cluster of the Max Planck Institute for Astronomy (MPIA), as well as the Cobra and Raven clusters, all three operated by the Max Planck Computational Data Facility (MPCDF); and the BinAC cluster, supported by the High Performance and Cloud Computing Group at the Zentrum für Datenverarbeitung of the University of Tübingen, the state of Baden-Württemberg through bwHPC and the German Research Foundation (DFG) through grant no INST 37/935-1 FUGG. The three original TNG simulations were run with compute time awarded by the Gauss Centre for Supercomputing (GCS) under GCS Large-Scale Projects GCS-ILLU and GCS-DWAR on the Hazel Hen supercomputer at the High Performance Computing Center Stuttgart (HLRS).

References

- Adam, R., Ricci, M., Eckert, D., et al. 2023, arXiv e-prints, arXiv:2310.05819
- Adami, C., Giles, P., Koulouridis, E., et al. 2018, *A&A*, 620, A5
- Ade, P., Aguirre, J., Ahmed, Z., et al. 2019a, *J. Cosmology Astropart. Phys.*, 2019, 056
- Ade, P., Aguirre, J., Ahmed, Z., et al. 2019b, *J. Cosmology Astropart. Phys.*, 2019, 056
- Agertz, O., Pontzen, A., Read, J. I., et al. 2020, *MNRAS*, 491, 1656
- Akino, D., Eckert, D., Okabe, N., et al. 2022, *PASJ*, 74, 175
- Allen, S. W., Evrard, A. E., & Mantz, A. B. 2011, *ARA&A*, 49, 409
- Altamara, E., Kay, S. T., Bower, R. G., et al. 2023, *MNRAS*, 520, 3164
- Amendola, L., Appleby, S., Avgoustidis, A., et al. 2018, *Living Reviews in Relativity*, 21, 2
- Anand, A., Kauffmann, G., & Nelson, D. 2022, *MNRAS*, 513, 3210
- Anders, E. & Grevesse, N. 1989, *Geochim. Cosmochim. Acta*, 53, 197
- Anderson, M. E., Gaspari, M., White, S. D. M., Wang, W., & Dai, X. 2015, *MNRAS*, 449, 3806
- Angulo, R. E., Springel, V., White, S. D. M., et al. 2012, *MNRAS*, 426, 2046
- Ardila, F., Huang, S., Leauthaud, A., et al. 2021, *MNRAS*, 500, 432
- Aricò, G., Angulo, R. E., Hernández-Monteagudo, C., Contreras, S., & Zennaro, M. 2021, *MNRAS*, 503, 3596
- Ayromlou, M., Kauffmann, G., Yates, R. M., Nelson, D., & White, S. D. M. 2021a, *MNRAS*, 505, 492
- Ayromlou, M., Nelson, D., & Pillepich, A. 2023a, *MNRAS*, 524, 5391
- Ayromlou, M., Nelson, D., Pillepich, A., et al. 2023b, arXiv e-prints, arXiv:2311.06339
- Ayromlou, M., Nelson, D., Yates, R. M., et al. 2021b, *MNRAS*, 502, 1051
- Ayromlou, M., Nelson, D., Yates, R. M., Kauffmann, G., & White, S. D. M. 2019, *MNRAS*, 487, 4313
- Babul, A., Balogh, M. L., Lewis, G. F., & Poole, G. B. 2002, *MNRAS*, 330, 329
- Bahé, Y. M., Barnes, D. J., Dalla Vecchia, C., et al. 2017, *MNRAS*, 470, 4186
- Bahé, Y. M. & McCarthy, I. G. 2015, *MNRAS*, 447, 969
- Barnes, D. J., Kay, S. T., Bahé, Y. M., et al. 2017a, *MNRAS*, 471, 1088
- Barnes, D. J., Kay, S. T., Henson, M. A., et al. 2017b, *MNRAS*, 465, 213
- Barnes, D. J., Vogelsberger, M., Kannan, R., et al. 2018, *MNRAS*, 481, 1809
- Barnes, D. J., Vogelsberger, M., Pearce, F. A., et al. 2021, *MNRAS*, 506, 2533
- Bassini, L., Rasia, E., Borgani, S., et al. 2020, *A&A*, 642, A37
- Bassini, L., Rasia, E., Borgani, S., et al. 2019, *A&A*, 630, A144
- Battaglia, N., Bond, J. R., Pfrommer, C., & Sievers, J. L. 2012, *ApJ*, 758, 74
- Bautz, M. W., Miller, E. D., Sanders, J. S., et al. 2009, *PASJ*, 61, 1117
- Behroozi, P., Wechsler, R. H., Hearin, A. P., & Conroy, C. 2019, *MNRAS*, 488, 3143
- Behroozi, P. S., Wechsler, R. H., & Conroy, C. 2013, *ApJ*, 770, 57
- Biffi, V., Dolag, K., & Böhringer, H. 2013, *MNRAS*, 428, 1395
- Biffi, V., Planelles, S., Borgani, S., et al. 2018, *MNRAS*, 476, 2689
- Blandford, R., Meier, D., & Readhead, A. 2019, *ARA&A*, 57, 467
- Bleem, L. E., Bocquet, S., Stalder, B., et al. 2020, *ApJS*, 247, 25
- Bogdán, Á., Lovisari, L., Volonteri, M., & Dubois, Y. 2018, *ApJ*, 852, 131
- Böhringer, H., Chon, G., & Kronberg, P. P. 2016, *A&A*, 596, A22
- Bonafede, A., Feretti, L., Murgia, M., et al. 2010, *A&A*, 513, A30
- Bonaventura, N. R., Webb, T. M. A., Muzzin, A., et al. 2017, *MNRAS*, 469, 1259
- Boselli, A., Fossati, M., Ferrarese, L., et al. 2018, *A&A*, 614, A56
- Botteon, A., Gastaldello, F., Brunetti, G., & Kale, R. 2016, *MNRAS*, 463, 1534
- Brunetti, G., Cassano, R., Dolag, K., & Setti, G. 2009, *A&A*, 507, 661
- Budzynski, J. M., Koposov, S. E., McCarthy, I. G., McGee, S. L., & Belokurov, V. 2012, *MNRAS*, 423, 104
- Bulbul, E., Chiu, I. N., Mohr, J. J., et al. 2019, *ApJ*, 871, 50
- Byrohl, C. & Nelson, D. 2023, *MNRAS*, 523, 5248
- Caglar, T., Koss, M. J., Burtscher, L., et al. 2023, arXiv e-prints, arXiv:2308.01800
- Calzadilla, M. S., McDonald, M., Donahue, M., et al. 2022, *ApJ*, 940, 140
- Carilli, C. L. & Taylor, G. B. 2002, *ARA&A*, 40, 319
- Cassano, R., Ettori, S., Brunetti, G., et al. 2013, *ApJ*, 777, 141
- Castignani, G., Pandey-Pommier, M., Hamer, S. L., et al. 2020, *A&A*, 640, A65
- Cavagnolo, K. W., Donahue, M., Voit, G. M., & Sun, M. 2008, *ApJ*, 683, L107
- Chadayammuri, U., Bogdán, Á., Oppenheimer, B. D., et al. 2022, *ApJ*, 936, L15
- CHEX-MATE Collaboration, Arnaud, M., Ettori, S., et al. 2021, *A&A*, 650, A104
- Chiu, I., Mohr, J. J., McDonald, M., et al. 2018, *MNRAS*, 478, 3072
- Choi, H. & Yi, S. K. 2017, *ApJ*, 837, 68
- Clowe, D., Bradač, M., Gonzalez, A. H., et al. 2006, *ApJ*, 648, L109
- Colberg, J. M., Krughoff, K. S., & Connolly, A. J. 2005, *MNRAS*, 359, 272
- Comparat, J., Truong, N., Merloni, A., et al. 2022, *A&A*, 666, A156
- Conroy, C., Wechsler, R. H., & Kravtsov, A. V. 2007, *ApJ*, 668, 826
- Crawford, C. S., Hatch, N. A., Fabian, A. C., & Sanders, J. S. 2005, *MNRAS*, 363, 216
- Cuciti, V., de Gasperin, F., Brüggen, M., et al. 2022, *Nature*, 609, 911
- Cui, W., Dave, R., Knebe, A., et al. 2022, *MNRAS*, 514, 977
- Cui, W., Knebe, A., Yepes, G., et al. 2018, *MNRAS*, 480, 2898
- Davis, M., Efstathiou, G., Frenk, C. S., & White, S. D. M. 1985, *ApJ*, 292, 371
- De Lucia, G. & Blaizot, J. 2007, *MNRAS*, 375, 2
- DeMaio, T., Gonzalez, A. H., Zabludoff, A., et al. 2020, *MNRAS*, 491, 3751
- Di Gennaro, G., van Weeren, R. J., Brunetti, G., et al. 2020, arXiv e-prints, arXiv:2011.01628
- Di Mascolo, L., Saro, A., Mroczkowski, T., et al. 2023, *Nature*, 615, 809
- Dolag, K., Komatsu, E., & Sunyaev, R. 2016, *MNRAS*, 463, 1797
- Domínguez-Fernández, P., Vazza, F., Brüggen, M., & Brunetti, G. 2019, *MNRAS*, 486, 623
- Donahue, M., Mack, J., Scharf, C., et al. 2001, *ApJ*, 552, L93
- Donahue, M. & Voit, G. M. 2022, *Phys. Rep.*, 973, 1
- Donnari, M., Pillepich, A., Joshi, G. D., et al. 2020a, arXiv e-prints, arXiv:2008.00005
- Donnari, M., Pillepich, A., Nelson, D., et al. 2020b, arXiv e-prints, arXiv:2008.00004
- Donnari, M., Pillepich, A., Nelson, D., et al. 2019, *MNRAS*, 485, 4817
- Dressler, A. 1980, *ApJ*, 236, 351
- D'Souza, R., Vegetti, S., & Kauffmann, G. 2015, *MNRAS*, 454, 4027
- Dunne, D. A., Webb, T. M. A., Noble, A., et al. 2021, *ApJ*, 909, L29
- Eckert, D., Ettori, S., Pointecouteau, E., et al. 2017, *Astronomische Nachrichten*, 338, 293
- Edge, A. C. 2001, *MNRAS*, 328, 762
- Ehlers, K., Weinberger, R., Pfrommer, C., Pakmor, R., & Springel, V. 2018, *MNRAS*, 481, 2878
- Eke, V. R., Navarro, J. F., & Frenk, C. S. 1998, *ApJ*, 503, 569
- Emsellem, E. 2013, *MNRAS*, 433, 1862
- Ettori, S., Baldi, A., Balestra, I., et al. 2015, *A&A*, 578, A46
- Evrard, A. E., Bialek, J., Busha, M., et al. 2008, *ApJ*, 672, 122
- Evrard, A. E., Summers, F. J., & Davis, M. 1994, *ApJ*, 422, 11
- Fabian, A. C. 2012, *ARA&A*, 50, 455
- Fabian, A. C., Sanders, J. S., Crawford, C. S., et al. 2003, *MNRAS*, 344, L48
- Fabian, A. C., Sanders, J. S., Ferland, G. J., et al. 2023, *MNRAS*, 521, 1794
- Ferrarese, L. 2002, *ApJ*, 578, 90
- Gaspari, M., Eckert, D., Ettori, S., et al. 2019, *ApJ*, 884, 169
- Genel, S., Vogelsberger, M., Nelson, D., et al. 2013, *MNRAS*, 435, 1426
- Genel, S., Vogelsberger, M., Springel, V., et al. 2014, *MNRAS*, 445, 175
- Ghizzardi, S., Molendi, S., van der Burg, R., et al. 2021, *A&A*, 646, A92
- Giacintucci, S., Markevitch, M., Cassano, R., et al. 2019, *ApJ*, 880, 70
- Giordini, S., Pierini, D., Finoguenov, A., et al. 2009, *ApJ*, 703, 982
- Giri, S. K. & Schneider, A. 2021, *J. Cosmology Astropart. Phys.*, 2021, 046

- Gitti, M., Brighenti, F., & McNamara, B. R. 2012, *Advances in Astronomy*, **2012**, 950641
- Gonzalez, A. H., Sivanandam, S., Zabludoff, A. I., & Zaritsky, D. 2013, *ApJ*, **778**, 14
- Govoni, F., Murgia, M., Vacca, V., et al. 2017, *A&A*, **603**, A122
- Grand, R. J. J., Springel, V., Gómez, F. A., et al. 2016, *MNRAS*, **459**, 199
- Guedes, J., Callegari, S., Madau, P., & Mayer, L. 2011, *ApJ*, **742**, 76
- Hadzhiyska, B., Ferraro, S., Pakmor, R., et al. 2023, *arXiv e-prints*, arXiv:2305.00992
- Hahn, O., Martizzi, D., Wu, H.-Y., et al. 2017, *MNRAS*, **470**, 166
- Hansen, S. M., Sheldon, E. S., Wechsler, R. H., & Koester, B. P. 2009, *ApJ*, **699**, 1333
- Henden, N. A., Puchwein, E., Shen, S., & Sijacki, D. 2018, *MNRAS*, **479**, 5385
- Hill, G. J., Kelz, A., Lee, H., et al. 2018, in Society of Photo-Optical Instrumentation Engineers (SPIE) Conference Series, Vol. 10702, Ground-based and Airborne Instrumentation for Astronomy VII, ed. C. J. Evans, L. Simard, & H. Takami, 107021K
- Hilton, M., Sifón, C., Naess, S., et al. 2020, *arXiv e-prints*, arXiv:2009.11043
- Hitomi Collaboration, Aharonian, F., Akamatsu, H., et al. 2018, *PASJ*, **70**, 9
- Hlavacek-Larrondo, J. & Fabian, A. C. 2011, *MNRAS*, **413**, 313
- Hlavacek-Larrondo, J., Li, Y., & Churazov, E. 2022, in Handbook of X-ray and Gamma-ray Astrophysics, 5
- Hoekstra, H., Herbonnet, R., Muzzin, A., et al. 2015, *MNRAS*, **449**, 685
- Hopkins, P. F., Wetzel, A., Kereš, D., et al. 2018, *MNRAS*, **480**, 800
- Iapichino, L. & Brüggen, M. 2012, *MNRAS*, **423**, 2781
- Jennings, F. & Davé, R. 2023, *arXiv e-prints*, arXiv:2306.01397
- Kaiser, N. 1986, *MNRAS*, **222**, 323
- Kannan, R., Vogelsberger, M., Pfrommer, C., et al. 2017, *ApJ*, **837**, L18
- Kartaltepe, J. S., Ebeling, H., Ma, C. J., & Donovan, D. 2008, *MNRAS*, **389**, 1240
- Katz, N. & White, S. D. M. 1993, *ApJ*, **412**, 455
- Kauffmann, G., White, S. D. M., Heckman, T. M., et al. 2004, *MNRAS*, **353**, 713
- Kay, S. T., Peel, M. W., Short, C. J., et al. 2012, *MNRAS*, **422**, 1999
- Kazantsev, A. P. 1968, Soviet Journal of Experimental and Theoretical Physics, **26**, 1031
- Kitayama, T., Ueda, S., Okabe, N., et al. 2023, *PASJ*, **75**, 311
- Knowles, K., Cotton, W. D., Rudnick, L., et al. 2022, *A&A*, **657**, A56
- Kormendy, J. & Ho, L. C. 2013, *ARA&A*, **51**, 511
- Kraft, R., Markevitch, M., Kilbourne, C., et al. 2022, *arXiv e-prints*, arXiv:2211.09827
- Kravtsov, A. V. & Borgani, S. 2012, *ARA&A*, **50**, 353
- Kravtsov, A. V., Vikhlinin, A. A., & Meshcheryakov, A. V. 2018, *Astronomy Letters*, **44**, 8
- Labbé, I., van Dokkum, P., Nelson, E., et al. 2023, *Nature*, **616**, 266
- Le Brun, A. M. C., McCarthy, I. G., Schaye, J., & Ponman, T. J. 2014, *MNRAS*, **441**, 1270
- Leauthaud, A., George, M. R., Behroozi, P. S., et al. 2012, *ApJ*, **746**, 95
- Leccardi, A. & Molendi, S. 2008, *A&A*, **487**, 461
- Lee, W., Pillepich, A., ZuHone, J., et al. 2023, *arXiv e-prints*, arXiv:2311.06340
- Lehle, K., Nelson, D., Pillepich, A., Truong, N., & Rohr, E. 2023, *arXiv e-prints*, arXiv:2311.06333
- Lewis, G. F., Babul, A., Katz, N., et al. 2000, *ApJ*, **536**, 623
- Lim, S. H., Barnes, D., Vogelsberger, M., et al. 2021, *MNRAS*, **504**, 5131
- Lin, Y.-T. & Mohr, J. J. 2004, *ApJ*, **617**, 879
- Lin, Y.-T., Mohr, J. J., & Stanford, S. A. 2004, *ApJ*, **610**, 745
- Lin, Y.-T., Stanford, S. A., Eisenhardt, P. R. M., et al. 2012, *ApJ*, **745**, L3
- Liska, M. T. P., Chatterjee, K., Issa, D., et al. 2022, *ApJS*, **263**, 26
- Liu, F. S., Mao, S., & Meng, X. M. 2012, *MNRAS*, **423**, 422
- Loosher, T. J., D'Eugenio, F., Maiolino, R., et al. 2023, *arXiv e-prints*, arXiv:2302.14155
- Lovell, C. C., Harrison, I., Harikane, Y., Tacchella, S., & Wilkins, S. M. 2023, *MNRAS*, **518**, 2511
- Lovisari, L., Forman, W. R., Jones, C., et al. 2017, *ApJ*, **846**, 51
- Lovisari, L. & Reiprich, T. H. 2019, *MNRAS*, **483**, 540
- Lovisari, L., Reiprich, T. H., & Schellenberger, G. 2015, *A&A*, **573**, A118
- Lovisari, L., Schellenberger, G., Sereno, M., et al. 2020, *ApJ*, **892**, 102
- Magorrian, J., Tremaine, S., Richstone, D., et al. 1998, *AJ*, **115**, 2285
- Malavasi, N., Sorce, J. G., Dolag, K., & Aghanim, N. 2023, *A&A*, **675**, A76
- Mantz, A. B., Allen, S. W., Morris, R. G., & von der Linden, A. 2018, *MNRAS*, **473**, 3072
- Mantz, A. B., Allen, S. W., Morris, R. G., et al. 2016, *MNRAS*, **463**, 3582
- Marasco, A., Cresci, G., Posti, L., et al. 2021, *MNRAS*, **507**, 4274
- Marinacci, F., Vogelsberger, M., Pakmor, R., et al. 2018, *MNRAS*, **480**, 5113
- Martín-Navarro, I., Pillepich, A., Nelson, D., et al. 2021, *Nature*, **594**, 187
- McCarthy, I. G., Balogh, M. L., Babul, A., Poole, G. B., & Horner, D. J. 2004, *ApJ*, **613**, 811
- McCarthy, I. G., Le Brun, A. M. C., Schaye, J., & Holder, G. P. 2014, *MNRAS*, **440**, 3645
- McCarthy, I. G., Schaye, J., Bird, S., & Le Brun, A. M. C. 2017, *MNRAS*, **465**, 2936
- McCarthy, I. G., Schaye, J., Bower, R. G., et al. 2011, *MNRAS*, **412**, 1965
- McConnell, N. J. & Ma, C.-P. 2013, *ApJ*, **764**, 184
- McDonald, M., Stalder, B., Bayliss, M., et al. 2016, *ApJ*, **817**, 86
- McNamara, B. R. & Nulsen, P. E. J. 2012, *New Journal of Physics*, **14**, 055023
- Merloni, A., Predehl, P., Becker, W., et al. 2012, *arXiv e-prints*, arXiv:1209.3114
- Mernier, F., de Plaa, J., Kaastra, J. S., et al. 2017, *A&A*, **603**, A80
- Mernier, F., Su, Y., Markevitch, M., et al. 2023, *arXiv e-prints*, arXiv:2310.04499
- Miralda-Escude, J. & Babul, A. 1995, *ApJ*, **449**, 18
- Molendi, S., Eckert, D., De Grandi, S., et al. 2016a, *A&A*, **586**, A32
- Molendi, S., Tozzi, P., Gaspari, M., et al. 2016b, *A&A*, **595**, A123
- Molnar, S. M., Hearn, N., Haiman, Z., et al. 2009, *ApJ*, **696**, 1640
- Montaña, A., Chávez Dagostino, M., Artxaga, I., et al. 2019, *Mem. Soc. Astron. Italiana*, **90**, 632
- Monteiro-Oliveira, R. 2022, *MNRAS*, **515**, 3674
- Montenegro-Taborda, D., Rodriguez-Gomez, V., Pillepich, A., et al. 2023, *MNRAS*, **521**, 800
- Moore, B., Katz, N., Lake, G., Dressler, A., & Oemler, A. 1996, *Nature*, **379**, 613
- Moster, B. P., Naab, T., & White, S. D. M. 2013, *MNRAS*, **428**, 3121
- Moster, B. P., Naab, T., & White, S. D. M. 2020, *MNRAS*, **499**, 4748
- Mroczkowski, T., Nagai, D., Basu, K., et al. 2019, *Space Sci. Rev.*, **215**, 17
- Nagai, D. 2006, *ApJ*, **650**, 538
- Nagarajan, A., Pacaud, F., Sommer, M., et al. 2019, *MNRAS*, **488**, 1728
- Naiman, J. P., Pillepich, A., Springel, V., et al. 2018, *MNRAS*, **477**, 1206
- Nandra, K., Barret, D., Barcons, X., et al. 2013, *arXiv e-prints*, arXiv:1306.2307
- Navarro, J. F., Frenk, C. S., & White, S. D. M. 1995, *MNRAS*, **275**, 720
- Nelson, D., Byrohl, C., Peroux, C., Rubin, K. H. R., & Burchett, J. N. 2021, *MNRAS*, **507**, 4445
- Nelson, D., Genel, S., Pillepich, A., et al. 2016, *MNRAS*, **460**, 2881
- Nelson, D., Kauffmann, G., Pillepich, A., et al. 2018a, *MNRAS*, **477**, 450
- Nelson, D., Pillepich, A., Springel, V., et al. 2019a, *MNRAS*, **490**, 3234
- Nelson, D., Pillepich, A., Springel, V., et al. 2018b, *MNRAS*, **475**, 624
- Nelson, D., Sharma, P., Pillepich, A., et al. 2020, *MNRAS*, **498**, 2391
- Nelson, D., Springel, V., Pillepich, A., et al. 2019b, *Computational Astrophysics and Cosmology*, **6**, 2
- Nelson, D., Vogelsberger, M., Genel, S., et al. 2013, *MNRAS*, **429**, 3353
- Nelson, K., Lau, E. T., & Nagai, D. 2014, *ApJ*, **792**, 25
- Niemiec, A., Julio, E., Limousin, M., et al. 2017, *MNRAS*, **471**, 1153
- Oñorbe, J., Garrison-Kimmel, S., Maller, A. H., et al. 2014, *MNRAS*, **437**, 1894
- Obuljen, A., Alonso, D., Villaescusa-Navarro, F., Yoon, I., & Jones, M. 2019, *MNRAS*, **486**, 5124
- O'Hara, T. B., Mohr, J. J., Bialek, J. J., & Evrard, A. E. 2006, *ApJ*, **639**, 64
- Okabe, N., Futamase, T., Kajisawa, M., & Kuroshima, R. 2014, *ApJ*, **784**, 90
- Olivares, V., Salome, P., Combès, F., et al. 2019, *A&A*, **631**, A22
- Orellheimer, B. D., Bogdán, Á., Crain, R. A., et al. 2020, *ApJ*, **893**, L24
- Orellana-González, G., Cerulo, P., Covone, G., et al. 2022, *MNRAS*, **512**, 2758
- Overzier, R. A. 2016, *A&A Rev.*, **24**, 14
- Pakmor, R., Bauer, A., & Springel, V. 2011, *MNRAS*, **418**, 1392
- Pakmor, R., Bieri, R., van de Voort, F., et al. 2023a, *arXiv e-prints*, arXiv:2309.13104
- Pakmor, R., Gómez, F. A., Grand, R. J. J., et al. 2017, *MNRAS*, **469**, 3185
- Pakmor, R., Marinacci, F., & Springel, V. 2014, *ApJ*, **783**, L20
- Pakmor, R. & Springel, V. 2013, *MNRAS*, **432**, 176
- Pakmor, R., Springel, V., Bauer, A., et al. 2016, *MNRAS*, **455**, 1134
- Pakmor, R., Springel, V., Coles, J. P., et al. 2023b, *MNRAS*, **524**, 2539
- Pasquali, A., Gallazzi, A., Fontanot, F., et al. 2010, *MNRAS*, **407**, 937
- Pearce, F. A., Kay, S. T., Barnes, D. J., Bahé, Y. M., & Bower, R. G. 2021, *MNRAS*, **507**, 1606
- Pellissier, A., Hahn, O., & Ferrari, C. 2023, *MNRAS*, **522**, 721
- Perotto, L., Adam, R., Ade, P., et al. 2022, in European Physical Journal Web of Conferences, Vol. 257, mm Universe @ NIKA2 - Observing the mm Universe with the NIKA2 Camera, 00038
- Pfrommer, C. & Jonathan Dursi, L. 2010, *Nature Physics*, **6**, 520
- Piffaretti, R., Arnaud, M., Pratt, G. W., Pointecouteau, E., & Melin, J. B. 2011, *A&A*, **534**, A109
- Pillepich, A., Nelson, D., Hernquist, L., et al. 2018a, *MNRAS*, **475**, 648
- Pillepich, A., Nelson, D., Springel, V., et al. 2019, *MNRAS*, **490**, 3196
- Pillepich, A., Porciani, C., & Reiprich, T. H. 2012, *MNRAS*, **422**, 44
- Pillepich, A., Sotillo-Ramos, D., Ramesh, R., et al. 2023, *arXiv e-prints*, arXiv:2303.16217
- Pillepich, A., Springel, V., Nelson, D., et al. 2018b, *MNRAS*, **473**, 4077
- Pinzke, A. & Pfrommer, C. 2010, *MNRAS*, **409**, 449
- Planck Collaboration. 2016, *A&A*, **594**, A13
- Planck Collaboration, Ade, P. A. R., Aghanim, N., et al. 2014, *A&A*, **571**, A20
- Poggianti, B. M., Moretti, A., Gullieuszik, M., et al. 2017, *ApJ*, **844**, 48
- Poole, G. B., Fardal, M. A., Babul, A., et al. 2006, *MNRAS*, **373**, 881
- Pop, A.-R., Hernquist, L., Nagai, D., et al. 2022, *arXiv e-prints*, arXiv:2205.11528
- Popesso, P., Biviano, A., Bulbul, E., et al. 2023, *arXiv e-prints*, arXiv:2302.08405
- Postman, M., Franx, M., Cross, N. J. G., et al. 2005, *ApJ*, **623**, 721
- Pratt, G. W., Croston, J. H., Arnaud, M., & Böhringer, H. 2009, *A&A*, **498**, 361
- Pulsoni, C., Gerhard, O., Arnaboldi, M., et al. 2020, *A&A*, **641**, A60

- Rafferty, D. A., McNamara, B. R., & Nulsen, P. E. J. 2008, [ApJ](#), **687**, 899
- Raghunathan, S., Whitehorn, N., Alvarez, M. A., et al. 2022, [ApJ](#), **926**, 172
- Ramesh, R., Nelson, D., Heesen, V., & Brüggen, M. 2023a, [MNRAS](#), [[arXiv:2305.11214](#)]
- Ramesh, R., Nelson, D., & Pillepich, A. 2023b, [MNRAS](#), **518**, 5754
- Randall, S. W., Sarazin, C. L., & Ricker, P. M. 2002, [ApJ](#), **577**, 579
- Rasia, E., Borgani, S., Murante, G., et al. 2015, [ApJ](#), **813**, L17
- Rasia, E., Ettori, S., Moscardini, L., et al. 2006, [MNRAS](#), **369**, 2013
- Reiprich, T. H., Basu, K., Ettori, S., et al. 2013, [Space Sci. Rev.](#), **177**, 195
- Reiprich, T. H., Veronica, A., Pacaud, F., et al. 2021, [A&A](#), **647**, A2
- Renneby, M., Henriques, B. M. B., Hilbert, S., et al. 2020, [MNRAS](#), **498**, 5804
- Riggs, S. D., Loveday, J., Thomas, P. A., et al. 2022, [MNRAS](#), **514**, 4676
- Rodriguez-Gomez, V., Genel, S., Vogelsberger, M., et al. 2015, [MNRAS](#), **449**, 49
- Rohr, E., Pillepich, A., Nelson, D., Ayromlou, M., & Zinger, E. 2023a, [arXiv e-prints](#), [[arXiv:2311.06337](#)]
- Rohr, E., Pillepich, A., Nelson, D., et al. 2023b, [MNRAS](#), **524**, 3502
- Romero, C. E., Mason, B. S., Sayers, J., et al. 2017, [ApJ](#), **838**, 86
- Roncarelli, M., Moscardini, L., Borgani, S., & Dolag, K. 2007, [MNRAS](#), **378**, 1259
- Rossetti, M., Gastaldello, F., Eckert, D., et al. 2017, [MNRAS](#), **468**, 1917
- Rossetti, M., Gastaldello, F., Feroli, G., et al. 2016, [MNRAS](#), **457**, 4515
- Sales, L. V., Vogelsberger, M., Genel, S., et al. 2015, [MNRAS](#), **447**, L6
- Salomé, P., Combes, F., Edge, A. C., et al. 2006, [A&A](#), **454**, 437
- Sato, T., Sasaki, T., Matsushita, K., et al. 2012, [PASJ](#), **64**, 95
- Schaal, K., & Springel, V. 2015, [MNRAS](#), **446**, 3992
- Schaye, J., Crain, R. A., Bower, R. G., et al. 2015, [MNRAS](#), **446**, 521
- Schaye, J., Kugel, R., Schaller, M., et al. 2023, [arXiv e-prints](#), [[arXiv:2306.04024](#)]
- Sembolini, F., Elahi, P. J., Pearce, F. R., et al. 2016, [MNRAS](#), **459**, 2973
- Sembolini, F., Yepes, G., De Petris, M., et al. 2013, [MNRAS](#), **429**, 323
- Serra, P., de Blok, W. J. G., Bryan, G. L., et al. 2016, in MeerKAT Science: On the Pathway to the SKA, 8
- Shin, T., Jain, B., Adhikari, S., et al. 2021, [MNRAS](#), **507**, 5758
- Sijacki, D., Vogelsberger, M., Genel, S., et al. 2015, [MNRAS](#), **452**, 575
- Simionescu, A., Allen, S. W., Mantz, A., et al. 2011, [Science](#), **331**, 1576
- Simionescu, A., Werner, N., Mantz, A., Allen, S. W., & Urban, O. 2017, [MNRAS](#), **469**, 1476
- Simionescu, A., ZuHone, J., Zhuravleva, I., et al. 2019, [Space Sci. Rev.](#), **215**, 24
- Smith, M. C., Sijacki, D., & Shen, S. 2019, [MNRAS](#), **485**, 3317
- Smith, R. K., Brickhouse, N. S., Liedahl, D. A., & Raymond, J. C. 2001, [ApJ](#), **556**, L91
- Sohn, J., Geller, M. J., Vogelsberger, M., & Damjanov, I. 2022, [ApJ](#), **931**, 31
- Springel, V. 2010, [MNRAS](#), **401**, 791
- Springel, V., Di Matteo, T., & Hernquist, L. 2005, [MNRAS](#), **361**, 776
- Springel, V., Pakmor, R., Pillepich, A., et al. 2018, [MNRAS](#), **475**, 676
- Springel, V., White, S. D. M., Tormen, G., & Kauffmann, G. 2001, [MNRAS](#), **328**, 726
- Steidel, C. C., Adelberger, K. L., Shapley, A. E., et al. 2000, [ApJ](#), **532**, 170
- Steinwandel, U. P., Dolag, K., Böss, L., & Marin-Gilabert, T. 2023, [arXiv e-prints](#), [[arXiv:2306.04692](#)]
- Stevens, A. R. H., Diemer, B., Lagos, C. d. P., et al. 2019, [MNRAS](#), **483**, 5334
- Stevens, A. R. H., Lagos, C. d. P., Cortese, L., et al. 2021, [MNRAS](#), **502**, 3158
- Sunyaev, R. A., & Zeldovich, Y. B. 1970, [Ap&SS](#), **7**, 3
- Tanigura, H., Zaroubi, S., & Aghanim, N. 2021, [A&A](#), **645**, A112
- Thomas, D., Maraston, C., Bender, R., & Mendes de Oliveira, C. 2005, [ApJ](#), **621**, 673
- Thomas, D., Maraston, C., Schawinski, K., Sarzi, M., & Silk, J. 2010, [MNRAS](#), **404**, 1775
- Tozzi, P., Gastaldello, F., Molendi, S., et al. 2015, [A&A](#), **580**, A6
- Tremmel, M., Quinn, T. R., Ricarte, A., et al. 2018, [ArXiv e-prints](#), [[arXiv:1806.01282](#)]
- Truong, N., Pillepich, A., Nelson, D., et al. 2023, [arXiv e-prints](#), [[arXiv:2311.06334](#)]
- Truong, N., Pillepich, A., & Werner, N. 2021, [MNRAS](#), **501**, 2210
- Truong, N., Pillepich, A., Werner, N., et al. 2020, [MNRAS](#) [[arXiv:1911.11165](#)]
- Valageas, P., & Silk, J. 1999, [A&A](#), **350**, 725
- van Daalen, M. P., Schaye, J., Booth, C. M., & Dalla Vecchia, C. 2011, [MNRAS](#), **415**, 3649
- van den Bosch, R. C. E., Gebhardt, K., Gültekin, K., et al. 2012, [Nature](#), **491**, 729
- van der Burg, R. F. J., Hoekstra, H., Muzzin, A., et al. 2015, [A&A](#), **577**, A19
- Vazza, F., & Brüggen, M. 2014, [MNRAS](#), **437**, 2291
- Vazza, F., Brunetti, G., Gheller, C., & Brunino, R. 2010, [New A](#), **15**, 695
- Vazza, F., Jones, T. W., Brüggen, M., et al. 2017, [MNRAS](#), **464**, 210
- Vazza, F., Wittor, D., Brunetti, G., & Brüggen, M. 2021, [A&A](#), **653**, A23
- Vikhlinin, A., Burenin, R. A., Ebeling, H., et al. 2009, [ApJ](#), **692**, 1033
- Vogelsberger, M., Genel, S., Springel, V., et al. 2014, [Nature](#), **509**, 177
- Vogelsberger, M., Marinacci, F., Torrey, P., et al. 2018, [MNRAS](#), **474**, 2073
- Voit, G. M., Balogh, M. L., Bower, R. G., Lacey, C. G., & Bryan, G. L. 2003, [ApJ](#), **593**, 272
- Voit, G. M., Donahue, M., Bryan, G. L., & McDonald, M. 2015, [Nature](#), **519**, 203
- Voit, G. M., Kay, S. T., & Bryan, G. L. 2005, [MNRAS](#), **364**, 909
- Voit, G. M., Oppenheimer, B. D., Bell, E. F., Terrazas, B., & Donahue, M. 2023, [arXiv e-prints](#), [[arXiv:2309.14818](#)]
- Wang, C., Li, R., Gao, L., et al. 2018a, [MNRAS](#), **475**, 4020
- Wang, J., Xu, D. W., & Wei, J. Y. 2018b, [ApJ](#), **852**, 26
- Wang, L., Dutton, A. A., Stinson, G. S., et al. 2015, [MNRAS](#), **454**, 83
- Wang, W., Sales, L. V., Henriques, B. M. B., & White, S. D. M. 2014, [MNRAS](#), **442**, 1363
- Webb, T. M. A., Muzzin, A., Noble, A., et al. 2015, [ApJ](#), **814**, 96
- Weinberger, R., Springel, V., Hernquist, L., et al. 2017, [MNRAS](#), **465**, 3291
- Werner, N., McNamara, B. R., Churazov, E., & Scannapieco, E. 2019, [Space Sci. Rev.](#), **215**, 5
- Wetzel, A., Hayward, C. C., Sanderson, R. E., et al. 2023, [ApJS](#), **265**, 44
- Wetzel, A. R., Tinker, J. L., Conroy, C., & van den Bosch, F. C. 2013, [MNRAS](#), **432**, 336
- Wu, K. K. S., Fabian, A. C., & Nulsen, P. E. J. 2000, [MNRAS](#), **318**, 889
- XRISM Science Team. 2020, [arXiv e-prints](#), [[arXiv:2003.04962](#)]
- Xu, H., Govoni, F., Murgia, M., et al. 2012, [ApJ](#), **759**, 40
- Yang, H.-Y. K., Ricker, P. M., & Sutter, P. M. 2009, [ApJ](#), **699**, 315
- Yates, R. M., Thomas, P. A., & Henriques, B. M. B. 2017, [MNRAS](#), **464**, 3169
- Yuan, F., & Narayan, R. 2014, [ARA&A](#), **52**, 529
- Yun, K., Pillepich, A., Zinger, E., et al. 2019, [MNRAS](#), **483**, 1042
- Zel'Dovich, Y. B. 1970, [A&A](#), **500**, 13
- Zhang, C., Churazov, E., Dolag, K., Forman, W. R., & Zhuravleva, I. 2020a, [arXiv e-prints](#), [[arXiv:2001.10959](#)]
- Zhang, H., Yang, X., Zaritsky, D., Behroozi, P., & Werk, J. 2020b, [ApJ](#), **888**, 33
- Zhang, Y. Y., Finoguenov, A., Böhringer, H., et al. 2008, [A&A](#), **482**, 451
- Zhang, Y.-Y., Okabe, N., Finoguenov, A., et al. 2010, [ApJ](#), **711**, 1033
- Zinger, E., Dekel, A., Kravtsov, A. V., & Nagai, D. 2018, [MNRAS](#), **475**, 3654
- Zinger, E., Joshi, G., Pillepich, A., Rohr, E., & Nelson, D. 2023, [arXiv e-prints](#), [[arXiv:2304.09202](#)]
- ZuHone, J. A., Kunz, M. W., Markevitch, M., Stone, J. M., & Biffi, V. 2015, [ApJ](#), **798**, 90
- ZuHone, J. A., Markevitch, M., & Lee, D. 2011, [ApJ](#), **743**, 16
- ZuHone, J. A., Vikhlinin, A., Tremblay, G. R., et al. 2023, SOXS: Simulated Observations of X-ray Sources, Astrophysics Source Code Library, record ascl:2301.024

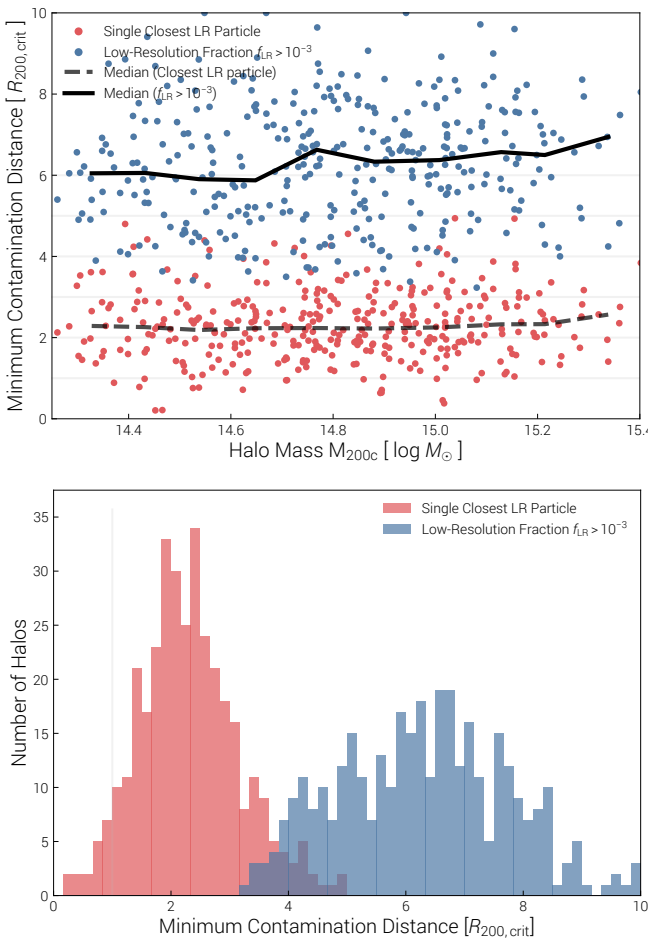


Fig. A.1. Numerical diagnostic of contamination of the high-resolution zoom regions in TNG-Cluster by lower resolution mass elements, at $z = 0$. **Top:** The minimum distance to the closest low-resolution dark matter particle from the center of each halo (red markers, dashed line), and the distance at which the low-resolution particle fraction exceeds one per thousand (blue markers, solid line). **Bottom:** Histograms of the number of halos with given minimum contamination radii, as measured by the single closest low-resolution dark matter particle (red) or as when the low-resolution particle fraction exceeds 10^{-3} (blue). A handful of halos have one or a few interloping low-resolution particles within one or two virial radii. However, the median distance out to which halos are more or less fully resolved by high-resolution particles is $\sim 4 - 8$ virial radii ($\gtrsim 5 - 10$ pMpc).

Appendix A: Technical Aspects

Figure A.1 explores the level of low-resolution ‘contamination’ in and near our target clusters. In any zoom simulation, the presence of low-resolution particles in the regions of interest (i.e. within the targeted halos) is undesirable and signifies a degradation of the numerical fidelity of the simulation (Oñorbe et al. 2014). Although not a strict boundary, distances out to which no, or little, contamination is present represent the volumes of interest when using TNG-Cluster.

For the fourteen halos with nonzero contamination within $1.0r_{\text{vir}}$, the median number of low resolution particles in that radius is just one, i.e. insignificant. The median distance out to which halos are more or less fully resolved by high-resolution particles is $\sim 3R_{200c}$ ($\gtrsim 4 - 5$ pMpc). However, if we relax our criterion to one low-resolution particle thousand, i.e. still insignificant, this distance roughly doubles. We also note that

contaminating particles are less and less of a concern at high redshift. For example, at $z = 7$, the ‘minimum contamination distances’ shift to $> 10R_{200c}$ for all halos. Contamination of the TNG-Cluster halos is not problematic.

By construction, large e.g. ~ 10 Mpc scale environmental effects, and large-scale projection effects (e.g. cosmological foregrounds or backgrounds along the lightcone) cannot be directly studied with TNG-Cluster. As designed, however, TNG-Cluster is well-suited not only for studies of the clusters themselves, but also their outskirts, nearby galaxy populations, and large-scale environments out to at least several virial radii.

Appendix B: The TNG-Cluster Catalog: physical properties and observables

Table B.1 presents the ‘TNG-Cluster Catalog’ where we collect a wide range of physical properties for each simulated galaxy cluster. These range from theoretical quantities such as formation redshift and dark matter halo concentration to observables such as X-ray luminosity or richness. Basic properties, such as halo mass and R_{500c} are accompanied by predictions for specific observational quantities with detailed forward-modeling pipelines.

This is a dynamic table which is available, and will be continually updated, online (www.tng-project.org/cluster). In particular, analyses from the other companion papers presenting first results from TNG-Cluster, as well as results from future publications, will be collected and unified. It is downloadable online in various machine readable formats.

ID [†]	Halo ID	M_{200c} log	M_{500c} log	R_{200c}	R_{500c}	$M_{\star,30\text{kpc}}$ log	M_{HI} log	$f_{\text{gas},500}$	SFR log	M_{SMBH} log	$L_{X,500}$ log	Y_{500} log	z_{form}	λ	CC?
-	-	[M_{\odot}]	[M_{\odot}]	[Mpc]	[Mpc]	[M_{\odot}]	[M_{\odot}]	-	[M_{\odot}/yr]	[M_{\odot}]	[erg/s]	[Mpc^2]	-	-	-
0	0	15.29	15.13	2.629	1.711	12.58	11.74	0.145	-	10.51	45.28	-3.86	0.49	248	CC
1	252455	15.40	15.27	2.871	1.912	12.16	11.37	0.126	-	9.35	44.96	-3.65	0.38	202	NCC
2	476245	15.16	14.99	2.378	1.541	12.16	11.82	0.132	-	10.17	44.59	-4.10	0.39	210	NCC
3	692426	15.36	15.14	2.782	1.731	12.53	11.55	0.149	-	10.19	45.06	-3.78	0.08	167	WCC
4	880597	14.94	14.71	2.018	1.248	12.14	11.66	0.136	-	9.64	44.51	-4.58	0.17	180	WCC
5	1068507	15.16	15.02	2.389	1.575	12.20	11.56	0.142	-	10.43	45.08	-4.01	0.57	178	WCC
6	1263653	15.34	15.08	2.730	1.654	12.42	11.22	0.130	-	10.41	44.66	-3.97	0.37	147	NCC
7	1431487	15.29	15.05	2.635	1.611	12.62	11.43	0.142	-	10.20	45.07	-4.02	0.12	151	WCC
8	1580995	15.36	15.19	2.779	1.799	12.52	11.37	0.149	-	10.60	45.30	-3.69	0.56	132	WCC
9	1763481	15.21	15.03	2.469	1.588	12.20	11.57	0.148	-	10.32	45.03	-3.98	0.35	149	WCC
10	1921024	15.23	15.03	2.509	1.589	12.40	11.49	0.144	-	10.38	44.90	-4.00	0.36	144	WCC
11	2069291	15.15	15.02	2.375	1.583	12.42	11.30	0.135	-	10.39	44.69	-4.06	0.60	120	NCC
12	2213486	15.29	15.11	2.626	1.689	12.34	11.43	0.146	-	10.38	45.07	-3.85	0.43	132	WCC
13	2380799	15.34	15.18	2.733	1.789	12.52	11.58	0.146	-	10.39	45.17	-3.76	0.42	110	WCC
14	2507618	15.32	15.17	2.694	1.774	12.43	11.56	0.151	2.68	10.65	45.49	-3.70	0.71	132	CC
15	2637623	15.20	15.07	2.465	1.645	12.56	11.60	0.139	-	10.45	44.91	-3.97	0.56	115	WCC
16	2771226	15.19	15.06	2.444	1.622	12.22	11.57	0.143	-	10.29	44.92	-3.99	0.35	126	WCC
17	2892630	15.28	15.18	2.620	1.788	12.39	11.46	0.142	-	10.53	45.14	-3.72	0.58	134	WCC
18	3020669	15.24	15.07	2.543	1.634	12.47	11.10	0.137	-	10.34	44.90	-3.97	0.33	94	WCC
19	3135769	15.19	14.97	2.448	1.515	12.47	11.68	0.152	2.71	10.37	45.45	-4.09	0.39	106	CC
20	3238091	15.09	14.94	2.256	1.489	12.40	11.64	0.146	-	10.40	45.19	-4.11	0.91	121	CC
21	3343359	15.27	15.08	2.598	1.655	12.43	11.30	0.147	-	10.51	45.20	-3.95	0.18	90	WCC
22	3457081	15.23	15.12	2.518	1.702	12.34	11.51	0.136	-	10.46	44.88	-3.90	0.60	112	NCC
23	3556542	15.25	15.04	2.548	1.601	12.35	11.10	0.131	-	10.11	44.59	-4.09	0.33	88	NCC
24	3656685	15.13	14.92	2.331	1.462	12.54	11.49	0.146	2.71	10.35	45.50	-4.14	0.39	97	CC
25	3758330	15.21	14.94	2.474	1.489	12.30	10.99	0.132	-	10.06	44.52	-4.21	0.29	114	NCC
26	3863281	15.24	15.13	2.537	1.723	12.23	11.18	0.147	-	10.25	45.35	-3.75	0.32	112	NCC
27	3960854	15.10	14.92	2.269	1.458	12.24	11.49	0.146	-	10.25	44.96	-4.20	0.26	108	WCC
28	4054274	15.21	14.99	2.485	1.547	12.28	11.16	0.142	-	10.13	45.07	-4.08	0.34	101	CC
29	4152102	15.20	15.06	2.455	1.622	12.54	11.25	0.138	-	10.31	44.97	-4.00	0.42	80	WCC
30	4254230	15.21	15.04	2.484	1.605	12.40	11.52	0.147	-	10.00	44.86	-4.03	0.19	115	WCC
31	4356618	15.21	15.09	2.478	1.664	12.52	11.07	0.138	-	10.53	45.16	-3.90	0.69	91	WCC
33	4461296	15.07	14.92	2.225	1.457	12.35	11.39	0.146	-	10.22	44.81	-4.19	0.45	90	WCC
34	4561713	15.11	14.98	2.300	1.531	12.23	11.36	0.140	-	9.83	45.11	-4.09	0.96	89	CC
35	4656216	15.18	15.00	2.418	1.548	12.53	11.02	0.142	-	10.30	44.67	-4.07	0.51	92	WCC
36	4753637	14.81	14.68	1.821	1.213	12.38	11.21	0.140	-	10.10	44.80	-4.57	0.77	115	WCC
37	4854863	15.13	14.98	2.330	1.536	12.52	11.35	0.148	-	10.38	45.30	-4.05	0.43	93	CC
38	4959833	15.16	15.02	2.378	1.577	12.59	11.77	0.141	-	10.33	45.26	-4.02	0.69	107	CC
39	5059214	15.09	14.92	2.262	1.458	12.50	11.23	0.143	2.72	10.23	45.02	-4.17	0.54	83	CC
40	5160063	15.15	14.95	2.367	1.497	11.94	11.69	0.142	-	9.60	45.18	-4.21	0.20	92	NCC
42	5251697	14.86	14.74	1.888	1.269	12.21	11.27	0.135	-	9.81	44.53	-4.51	0.48	65	NCC
44	5348819	15.01	14.57	2.128	1.119	12.01	11.10	0.116	-	9.65	44.33	-4.84	0.12	71	WCC
45	5432141	15.10	14.97	2.273	1.517	12.30	11.57	0.142	-	10.28	44.82	-4.10	0.56	93	WCC
...
4274	19372389	14.31	14.16	1.244	0.816	11.81	11.23	0.128	-0.61	9.53	43.67	-5.47	0.63	24	WCC
4369	19389199	14.30	13.99	1.234	0.716	11.73	11.02	0.102	-	9.33	43.18	-5.78	0.22	18	WCC
4394	19402069	14.31	14.13	1.237	0.800	11.80	9.35	0.130	-	9.65	43.75	-5.50	0.77	15	WCC
4414	19416927	14.35	14.21	1.279	0.847	11.62	11.05	0.119	-	9.02	43.60	-5.43	0.18	15	WCC
5122	19429412	14.26	14.00	1.195	0.719	11.71	10.47	0.118	-	9.24	43.37	-5.74	0.23	12	WCC
5711	19441351	14.31	14.19	1.241	0.837	11.92	10.39	0.132	-	9.63	43.89	-5.42	1.00	8	WCC

Table B.1. Selection of physical properties of the primary TNG-Cluster sample. Each of the 352 clusters is given as a single row. All values are quoted at $z = 0$ unless specified otherwise, and galaxy properties are provided for the central/BCG of each halo. The columns are: ID[†] the original Halo ID (from the parent simulation), Halo ID (in TNG-Cluster), halo mass M_{200c} , halo mass M_{500c} , virial radius R_{200c} , R_{500c} , stellar mass measured within a 30 pkpc aperture, neutral HI gas mass in the halo, gas fraction within R_{500c} , star formation rate ('-' denotes an upper limit of $< 10^{-3} \text{ M}_{\odot}\text{yr}^{-1}$), SMBH mass, X-ray luminosity within R_{500c} in the 0.5 – 2 keV soft-band, integrated Sunyaev-Zeldovich y-parameter within R_{500c} (both 3D spherical apertures), formation redshift, richness defined as the number of satellite galaxies with $M_{\star} > 10^{10.5} \text{ M}_{\odot}$, and cool-core state (CC for cool-core, WCC for weak cool-core, and NCC for non-cool core halos, from Lehle et al. 2023, as an example). This is a **dynamic, online table which contains many additional properties**. We will continually update this ‘TNG-Cluster Catalog’ with specialized and contributed analyses. The full, unabridged table is available for download online in various formats.